

Multi-objective calibration of elastic-viscoplastic models to capture the elevated-temperature creep and tensile behaviour of alloy 617

J. Choi ^{a,b}, O. Muránsky ^{a,b,*} , M.C. Messner ^c, J.J. Kruzic ^b, M.D. McMurtrey ^d

^a Australian Nuclear Science and Technology Organisation (ANSTO), Lucas Heights, NSW, Australia

^b School of Mechanical and Manufacturing Engineering, University of New South Wales (UNSW Sydney), Sydney, NSW, 2052, Australia

^c Applied Materials Division, Argonne National Laboratory, Lemont, IL, 60439, USA

^d Idaho National Laboratory, Idaho Falls, ID, 83415, USA



ABSTRACT

High-temperature engineering systems are expected to operate under sustained thermal and mechanical loads while also undergoing repeated thermal transients. Consequently, it is essential to develop material models capable of accurately predicting behaviour under a range of loading and temperature conditions. This study presents a multi-objective calibration framework for semi-empirical elastic-viscoplastic (EVP) models, aimed at simultaneously capturing the creep and tensile behaviour of Alloy 617 at 800°C, 900°C, and 1000°C. A three-stage calibration workflow was developed using a multi-objective genetic algorithm (MOGA) to identify a unified set of material parameters for two EVP-based models: (i) one incorporating classical creep damage (EVP-CD), and (ii) another incorporating work-based damage (EVP-WD). Both models were calibrated using short-term high-temperature creep and tensile datasets while their validation was performed against longer-term creep datasets obtained at a given temperature. The results demonstrate that the calibrated material models can capture both high-temperature creep and tensile behaviour. Notably, the EVP-WD model exhibited better accuracy in reproducing the full tensile stress-strain response to failure, albeit with greater calibration difficulty. The proposed approach paves the way for the development of a single material model applicable to multiple service conditions, thereby simplifying and improving the accuracy of fitness-for-service assessments of high-temperature engineering components.

1. Introduction

Alloy 617 is a solid-solution strengthened, nickel-based alloy with applications in elevated-temperature systems across various industries [1]. For instance, it is used in combustion cans and transition liners of aircraft as well as land-based gas turbines. The nuclear industry is also pursuing Alloy 617 for intermediate heat exchangers in the next generation (Gen. IV) of nuclear reactor systems, such as very high-temperature reactor (VHTR) systems. These advanced reactor systems are designed to cogenerate electricity and industrial heat for decarbonisation of heavy industries, such as steel, cement, and fertiliser production [2–4]. As a result, they are expected to operate at significantly higher temperatures (750°C) than the current fleet of nuclear reactor systems (300°C) [3]. To address this challenge, the American Society of Mechanical Engineers (ASME) recently incorporated Alloy 617 into ASME Section III, Division 5 of the Boiler Pressure and Vessel Code (BPVC), facilitating its use in advanced reactor systems. Under the current ASME code, Alloy 617 can be used in nuclear power applications at temperatures of up to 954°C with a service time limit of 100,000 h (~11.4 years) [5]. Since nuclear reactors are expected to operate for decades [6], it is essential to refine the current design framework by

developing a deeper understanding of the high-temperature deformation and degradation of Alloy 617, particularly under creep and tensile loads. Notably, this can be achieved through material models, which can predict material behaviour under various loading conditions without the need for extensive experimental testing, thereby accelerating the standardisation of new materials.

Empirical material models, such as Norton's power law [7], the Larson-Miller method [8], and the Manson-Haferd method [9], are characterised by their simple definitions and low computational costs [10]. However, these models often struggle to accurately describe the ongoing deformation and degradation mechanics of materials under operating in-service conditions. Furthermore, these models are prone to over-conservatism and poor extrapolations beyond tested scenarios [10, 11]. Semi-empirical material models improve upon empirical models by incorporating the underlying physical mechanisms that govern material behaviour under elevated temperature and stress conditions. This enables semi-empirical models to more reliably extrapolate beyond test conditions, capture mechanism shifts, and accommodate different loading scenarios. Well-established examples include the Kachanov-Rabotnov [12,13] model, ductility exhaustion models [14–16], and elastic-viscoplastic (EVP) models [17,18]. However, the main challenge when using semi-empirical models lies in their

* Corresponding author. Australian Nuclear Science and Technology Organisation (ANSTO), Lucas Heights, NSW, Australia.

E-mail address: ondrej.muransky@ansto.gov.au (O. Muránsky).

Nomenclature	
<i>Creep- and tensile-related parameters</i>	
C	= Isotropic elasticity tensor
E	= Elastic modulus
I	= Identity tensor
t	= Time
t_f	= Creep time-to-failure
T	= Temperature
ν	= Poisson's ratio
ϵ	= Strain
ϵ_{area}	= Total creep strain (area under creep curve)
ϵ_d	= Tensile strain-at-ductility
ϵ_e	= Elastic strain tensor
ϵ_f	= Creep strain-to-failure
$\dot{\epsilon}_{min}$	= Minimum creep rate
ϵ_{vp}	= Viscoplastic strain tensor
σ	= Stress
σ	= Stress tensor
σ_{area}	= Toughness (area under tensile curve)
σ_d	= Tensile stress-at-ductility
σ_{MTS}	= Maximum true stress
σ_{UTS}	= Ultimate tensile stress
σ_y	= Tensile yield stress
<i>Elastic-viscoplastic model material parameters</i>	
d_{VIH}	= Isotropic hardening rate
n_{PF}	= Flow surface exponent
R_{VIH}	= Isotropic hardening modulus
η_{PF}	= Viscoplastic fluidity parameter
$\sigma_{y,0}$	= Initial yield stress
<i>Creep damage model material parameters</i>	
A_{CD}	= Stress prefactor
ξ_{CD}	= Stress power law exponent
ϕ_{CD}	= Damage power law exponent
<i>Work damage model material parameters</i>	
a_{WD}	= Creep critical work density intercept
A_{WD}	= Creep critical work density gradient
b_{WD}	= Tensile critical work density intercept
B_{WD}	= Tensile critical work density gradient
α_{WD}	= Creep damage exponent
β_{WD}	= Tensile damage exponent
<i>Miscellaneous parameters</i>	
f_{PF}	= Perzyna yield function
J_2	= Deviatoric stress invariant
n_d	= Damage exponent
W	= Plastic work density
W_{crit}	= Critical plastic work density
λ_1	= Work density rate threshold for decay
λ_2	= Work density rate threshold for transition
σ_h	= Hardening stress
ω	= Damage state variable
<i>Creep objective functions</i>	
E_{t_f}	= Objective function for time-to-failure
$E_{\epsilon_{area}}$	= Objective function for strain values
E_{ϵ_f}	= Objective function for strain-to-failure
$E_{\dot{\epsilon}_{min}}$	= Objective function for minimum creep rate
<i>Tensile objective functions</i>	
E_{ϵ_d}	= Objective function for strain-at-ductility
$E_{\sigma_{area}}$	= Objective function for stress values
$E_{\sigma_{MTS}}$	= Objective function for maximum true stress
E_{σ_y}	= Objective function for yield stress

calibration, which involves finding the set of unknown material parameters that best describes the experimentally observed material response.

Traditionally, manual trial-and-error methods were employed to calibrate material models. However, these methods were often subjective, time-consuming, and heavily dependent on prior knowledge of the material parameters. As such, gradient-based and direct-search optimisation methodologies are often employed to automate and streamline the calibration process of semi-empirical models [10,19]. Gradient-based optimisation methods, such as gradient descent, Adam, and Newton-type methods, are efficient and well-suited for high-dimensional problems [20,21]. However, these methods rely heavily on the initial parameter values and often converge towards local minima, particularly in the complex and non-linear parameter spaces characteristic of semi-empirical models [21,22]. Gradient-based methods also require differentiability in their objective functions, in which noise in the experimental data could deteriorate convergence behaviour [22]. In contrast, direct-search optimisation methods do not rely on gradient information, making them generally more robust and better suited for exploring diverse regions of large parameter spaces [10, 23]. A notable example is the genetic algorithm (GA), which has been widely used in the calibration of complex material models due to its effectiveness at locating global minima and simultaneous handling of multiple objective functions [10,22,24–26]. However, despite these advantages, direct-search methods typically require a substantial number of evaluations to achieve convergence.

In the present work, a novel three-stage multi-objective calibration workflow was developed using a multi-objective genetic algorithm

(MOGA) to efficiently calibrate two semi-empirical material models to capture the elevated-temperature creep and tensile behaviour of Alloy 617. The semi-empirical models employed a temperature-dependent elastic-viscoplastic (EVP) constitutive model, coupled with either a classical creep damage (CD) or work-based damage (WD) model to capture the failure response. The calibration of the EVP-CD and EVP-WD models was performed against high-temperature experimental creep and tensile datasets collected by the Idaho National Laboratory (INL) [27] as a part of the ASME code case. The calibration workflow involved 1) determining the material parameters for the EVP model, 2) identifying the parameters for the damage models (CD, WD), and subsequently 3) fine-tuning the parameters together. The models were calibrated using the short-term creep and tensile datasets and validated using longer-term creep datasets. This approach allowed the assessment of the models' accuracy in extrapolating beyond the calibration datasets, thereby evaluating their predictive capabilities. From these assessments, it is shown that both damage models can capture high-temperature creep and tensile yielding behaviour, with the WD model producing more accurate tensile stress-strain curves to failure at the cost of being more difficult to calibrate.

2. Experimental data

Alloy 617 is a solid-solution strengthened, Cr-Co-Mo nickel-based alloy [16], known for its exceptional oxidation resistance, toughness, and high-temperature strength [28]. To support the certification of Alloy 617 for high-temperature nuclear pressure vessel applications, Idaho National Laboratory (INL) conducted a comprehensive suite of creep

and tensile tests at various temperature-stress conditions [5,27,29]. These tests were performed on an as-received, solution-annealed plate of Alloy 617 Heat 314626 manufactured by ThyssenKrupp Vereinigte Deutsch Metallwerke (VDM) [30]. The chemical composition of the Alloy 617 plate is listed in Table 1.

The creep tests were performed in accordance with ASTM E139-11 [31] under constant temperature and uniaxial stress conditions at 800°C (60MPa, 65MPa, 70MPa, 80MPa), 900°C (26MPa, 28MPa, 31MPa, 36MPa), and 1000°C (11MPa, 12MPa, 13MPa, 16MPa). The tensile tests were performed following ASTM E8-11 [32] under the same constant temperature conditions at 800°C, 900°C, and 1000°C. The minimum strain rate observed during the creep testing ranged between $9.9 \times 10^{-6}\text{s}^{-1}$ and $2.4 \times 10^{-4}\text{s}^{-1}$, while all the tensile tests were performed under a constant strain rate of approximately 10^{-4}s^{-1} . The experimental data obtained from these tests were made available by INL to support the calibration and validation of the semi-empirical material models. The experimental creep and tensile data used in this study is presented in Fig. 1. The experimental creep data is employed in the form of strain-time creep curves to failure, with each annotated with the minimum creep rate ($\dot{\epsilon}_{min}$), time-to-failure (t_f), and strain-to-failure (ϵ_f). The experimental tensile data is employed in the form of stress-strain tensile curves up to 80% of the maximum true stress (i.e., stress-at-ductility), with each annotated with the yield stress (σ_y), maximum true stress (σ_{MTS}), the strain-at-ductility (ϵ_d), and the stress-at-ductility (σ_d). Note that the tensile data was originally provided in engineering stress-strain values and converted to homogeneous true stress-strain values using standard relations. The experimental conditions of the creep and tensile tests are summarised in Appendix A.

The creep curves in Fig. 1 show that the creep life of Alloy 617 is predominantly in the secondary and tertiary creep regimes, with a limited amount in the primary creep regime. Additionally, some of the creep curves exhibit atypical behaviour characterised by a decreasing strain rate in the tertiary regime. This behaviour is visible in the creep curves at 900°C (26MPa) and 1000°C (11MPa, 12MPa, 13MPa, 16MPa), and is attributed to the creep tests being conducted in air, causing significant surface oxidation [33–35]. Since oxidation is a diffusion-controlled process, the effects of the surface oxidation are more pronounced at lower stresses as these lead to longer exposure times [34].

The experimental creep and tensile data were processed to support the calibration of the semi-empirical models, by reducing noise and ensuring compatibility with the modelling frameworks. Specifically, fluctuations in the experimental extensometer and thermocouple data were filtered out from the experimental data using the Savitzky-Golay filter. Filtering the data stabilised the optimisation results by enabling the optimiser to more easily discern underlying trends and patterns in the data. The atypical tertiary behaviour caused by the surface oxidation was also removed from the affected creep curves by excluding the data beyond the inflection corresponding to the maximum strain rate (where the curvature changes signs from positive to negative), as shown in Fig. 1. This was done to assess the typical prediction capabilities of the semi-empirical models, which were not designed to capture the effects of oxidation.

3. Elastic-viscoplastic material models

Semi-empirical models combine theoretical principles with the existing experimental datasets to describe material behaviour under varying loading conditions. By considering the underlying deformation

and degradation mechanisms, semi-empirical models can reliably extrapolate beyond test conditions, capture mechanism shifts, and accommodate different loading scenarios. One of the most popular semi-empirical models is the elastic-viscoplastic (EVP) model [17,18], which describes the time-dependent plastic behaviour as attributed to the motion of dislocations, formation of cavities, and the sliding of grain boundaries [36]. While the EVP model is unable to capture damage by itself, it can be readily coupled with a classical creep damage (CD) model or a work damage (WD) model to capture the material's entire service life. Both the EVP-CD and EVP-WD models were implemented using the nuclear engineering material model library (NEML) [37]. For the creep simulations, the models were terminated when the damage reached a value of 0.95; for the tensile simulations, the models were terminated when the stress dropped to 80% of the maximum true stress (i.e., stress-at-ductility). The following section defines the EVP model (section 3.1) and its coupling with the CD model (section 3.2) and WD model (section 3.3). Additionally, a summary of the material parameters for the EVP, CD, and WD models can be found in Appendix B.

3.1. Definition of elastic-viscoplastic model

In this study, the elastic-viscoplastic (EVP) model was employed to characterise deformation behaviour under high-temperature loading by coupling elastic and viscoplastic mechanisms. The model is formulated within the infinitesimal strain framework [38–40], where the total strain rate ($\dot{\epsilon}$) of the material is additively decomposed into second order tensors of the elastic strain rate ($\dot{\epsilon}_e$) and viscoplastic strain rate ($\dot{\epsilon}_{vp}$), as expressed in Eq. (1). It is acknowledged that the experimental creep and tensile data used in this study (section 2) involve strains of up to 64.1%, which exceeds the validity limit of the infinitesimal strain theory. While a finite strain formulation would offer a more rigorous approach for modelling large deformations, the infinitesimal strain approach was adopted to reduce computational complexity and ensure compatibility with existing model formulations.

$$\dot{\epsilon} = \dot{\epsilon}_e + \dot{\epsilon}_{vp} \quad (1)$$

In this study, elastic deformation is assumed to be isotropic, and as such, the elastic component of the proposed EVP model can be represented by the conventional form of Hooke's law. This is shown in Eq. (2), where $\dot{\sigma}$ represents the stress rate and C represents the isotropic elasticity tensor described by the elastic modulus (E) and Poisson's ratio (ν).

$$\dot{\sigma} = C : \dot{\epsilon}_e \quad (2)$$

The expanded matrix form of the employed Hooke's law is shown in Eq. (3).

$$\begin{bmatrix} \dot{\sigma}_{11} \\ \dot{\sigma}_{22} \\ \dot{\sigma}_{33} \\ \dot{\sigma}_{23} \\ \dot{\sigma}_{13} \\ \dot{\sigma}_{12} \end{bmatrix} = \frac{E}{(1+\nu)(1-2\nu)} \begin{bmatrix} 1-\nu & \nu & \nu & 0 & 0 & 0 \\ \nu & 1-\nu & \nu & 0 & 0 & 0 \\ \nu & \nu & 1-\nu & 0 & 0 & 0 \\ 0 & 0 & 0 & \frac{1-2\nu}{2} & 0 & 0 \\ 0 & 0 & 0 & 0 & \frac{1-2\nu}{2} & 0 \\ 0 & 0 & 0 & 0 & 0 & \frac{1-2\nu}{2} \end{bmatrix} \begin{bmatrix} \dot{\epsilon}_{e,11} \\ \dot{\epsilon}_{e,22} \\ \dot{\epsilon}_{e,33} \\ \dot{\epsilon}_{e,23} \\ \dot{\epsilon}_{e,13} \\ \dot{\epsilon}_{e,12} \end{bmatrix} \quad (3)$$

The viscoplastic component of the EVP model is represented by the Perzyna viscoplastic flow rule [41] within a power-law framework,

Table 1

Chemical composition of solution-annealed plate of Alloy 617 Heat 314626 in weight percent [27].

Ni	Cr	Co	Mo	Al	Ti	Fe	Mn	Cu	Si	C	S	B
54.1	22.2	11.6	8.6	1.1	0.4	1.6	0.1	0.04	0.1	0.05	<0.002	<0.001

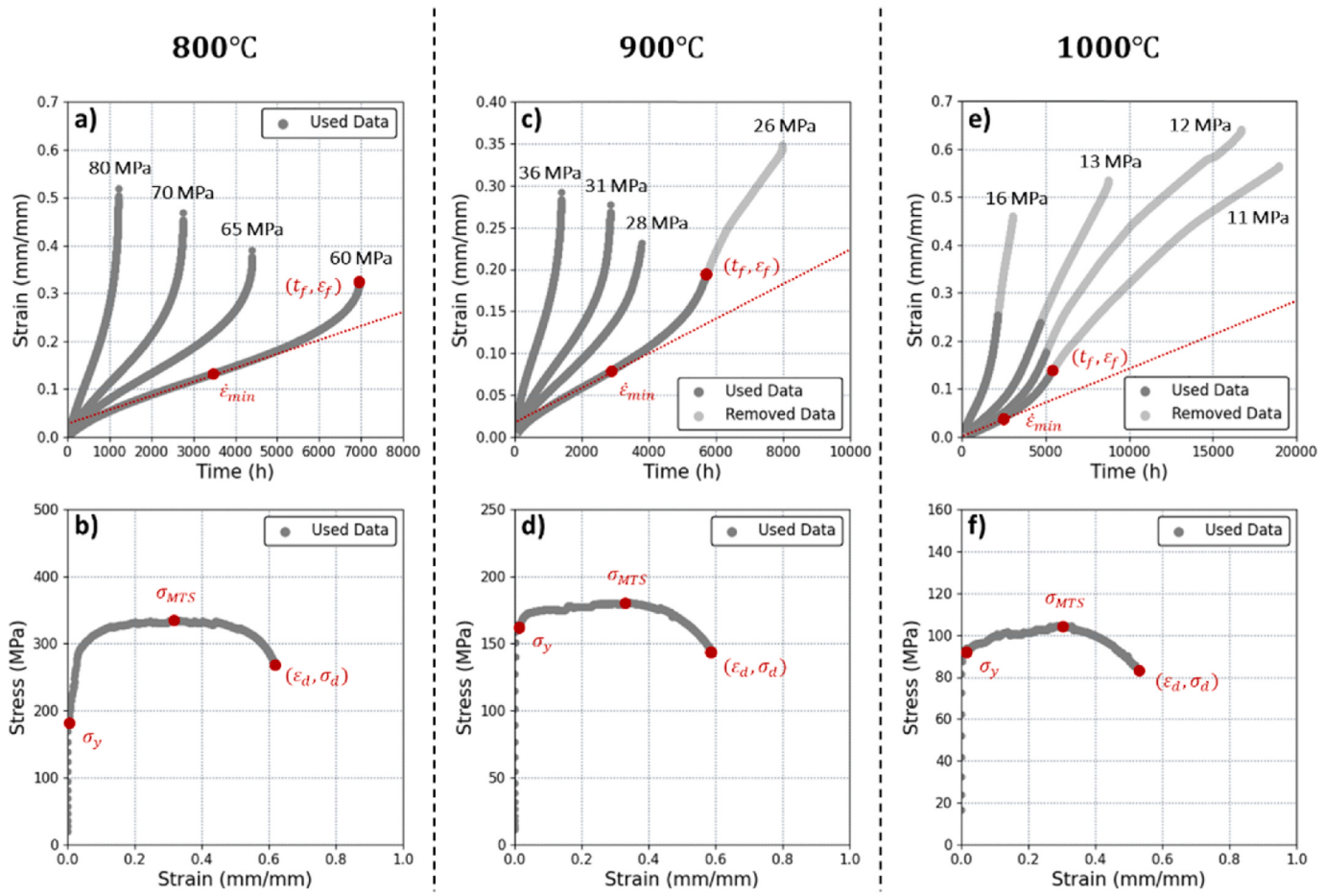


Fig. 1. Annotated plots of the experimental data of Alloy 617 from the Idaho National Laboratory. Plots in a), c), and e) are of the experimental creep data at 800°C, 900°C, and 1000°C, respectively. Plots in b), d), and f) are of the experimental tensile data at 800°C, 900°C, and 1000°C, respectively.

which relates the viscoplastic strain rate ($\dot{\epsilon}_{vp}$) to the applied stress (σ) and two temperature-dependent material parameters. The viscoplastic model is defined in Eq. (4) [41], where f_{PF} is the yield function, n_{PF} represents the flow surface exponent, and η_{PF} represents the viscosity parameter.

$$\dot{\epsilon}_{vp} = \left(\frac{\langle f_{PF}(\sigma, \sigma_h, T) \rangle}{\eta_{PF}} \right)^{n_{PF}} \quad (4)$$

The $\langle \cdot \rangle$ notation in Eq. (4) represents the McCauley brackets. The definition of $\langle x \rangle$ for a value x is defined by the expression in Eq. (5) [41].

$$\langle x \rangle = \begin{cases} 0, & x < 0 \\ x, & x \geq 0 \end{cases} \quad (5)$$

The yield function (f_{PF}) from Eq. (4) is defined by the expression in Eq. (6). In this expression, J_2 represents the deviatoric stress invariant, T represents the temperature, σ represents the applied stress, and σ_h represents the hardening stress [38].

$$f_{PF}(\sigma, \sigma_h, T) = J_2(\sigma) + \sqrt{\frac{2}{3}}\sigma_h \quad (6)$$

The J_2 function describes the von Mises effective stress [38], and is defined in Eq. (7).

$$J_2(\sigma) = \sqrt{\frac{3}{2}\text{dev}(\sigma) : \text{dev}(\sigma)} \quad (7)$$

The dev notation in Eq. (7) denotes the deviator function. The definition of $\text{dev}(\mathbf{X})$ for some second order tensor \mathbf{X} is shown in Eq. (8), where tr is the trace, and \mathbf{I} is the identity tensor.

$$\text{dev}(\mathbf{X}) = \mathbf{X} - \frac{1}{3}\text{tr}(\mathbf{X})\mathbf{I} \quad (8)$$

In addition to isotropic elastic behaviour, the material is assumed to exhibit isotropic viscoplastic behaviour. Hence, the hardening stress (σ_h) is obtained using the Voce isotropic hardening rule [42], as defined by the expression in Eq. (9). In this expression, $\sigma_{y,0}$ represents the initial yield stress, R_{VIH} represents the isotropic hardening modulus, and d_{VIH} represents the isotropic hardening rate [43]. Note that d_{VIH} controls the rate of hardening whereas R_{VIH} controls the magnitude of the hardening [44].

$$\sigma_h = \sigma_{y,0} + R_{VIH}(1 - e^{-d_{VIH}/\dot{\epsilon}_{vp}}) \quad (9)$$

Once combined, the EVP model contains five material parameters. The first three parameters ($\sigma_{y,0}$, R_{VIH} , and d_{VIH}) come from the Voce isotropic hardening rule [42], whereas the remaining parameters (n_{PF} and η_{PF}) come from the Perzyna viscoplastic flow rule [41]. The values of these parameters must be calibrated for the EVP model to capture the deformation behaviour of Alloy 617.

3.2. Coupling with a classical creep damage model

The elastic-viscoplastic creep damage (EVP-CD) model couples the EVP model with the Hayhurst-Leckie-Kachanov-Rabotnov creep damage (CD) model [45], which characterises damage accumulation based on the local reduction in the material's cross-sectional area, as a function of time. The CD model relies on a damage state variable, ω , such that $\omega = 0$

when the material is in its undamaged state and $\omega = 1$ when the material is ruptured. In the CD model, ω is defined by Eq. (10), where A_{CD} represents the stress prefactor, ξ_{CD} represents the stress power law exponent, and ϕ_{CD} represents the damage power law exponent [46]. For this study, the effective stress is defined by the J_2 function described in Eq. (7).

$$\dot{\omega} = \left(\frac{J_2(\sigma)}{A_{CD}} \right)^{\xi_{CD}} (1 - \omega)^{\xi_{CD} - \phi_{CD}} \quad (10)$$

The addition of the CD model introduces three material parameters (A_{CD} , ξ_{CD} , and ϕ_{CD}), which results in the coupled EVP-CD model having a total of eight material parameters.

3.3. Coupling with a work damage model

The elastic-viscoplastic work damage (EVP-WD) model couples the EVP model with the work damage (WD) model. The WD model shares functionality with ductility exhaustion models [14–16] that evaluate material failure based on ductility decline but differ in their characterisation of damage as a function of plastic work density rather than strain. In the WD model, the damage state variable, ω , is defined by Eq. (11), where W represents the plastic work density, W_{crit} represents the critical plastic work density, and n_d represents the damage exponent that controls the onset of damage in the material flow stress.

$$\dot{\omega} = \frac{n_d \omega^{\frac{n_d-1}{n_d}} \dot{W}}{W_{crit}} \quad (11)$$

The WD model defines the critical work density (W_{crit}) and the damage exponent (n_d) as piecewise functions of the logarithmised work density rate (i.e., $\log_{10}(\dot{W})$) controlled by six parameters (A_{WD} , a_{WD} , B_{WD} , b_{WD} , α_{WD} , and β_{WD}), resulting in the coupled EVP-WD model having a total of eleven material parameters. The critical work density is represented as a bilinear function, where A_{WD} and a_{WD} control the linear relationship for creep and B_{WD} and b_{WD} control the linear relationship for tensile. The damage exponent is represented as a step function where α_{WD} and β_{WD} represent the damage exponent values for creep and tensile, respectively. These representations were inspired by the relationship of the critical work density and average work density rate in the experimental creep and tensile data, from which the values of A_{WD} , a_{WD} , B_{WD} , and b_{WD} were calculated to be 15.063s, 103.03MPa, 264.45s, and 599.01MPa. As such, $A_{WD} < B_{WD}$ and $a_{WD} < b_{WD}$ are enforced to preserve the experimentally observed relationship. The critical work density and

damage exponent functions are discussed in further depth in Appendix C.

4. Methodology

The semi-empirical models must be calibrated before they can be used to capture creep and tensile behaviour. In this study, the EVP-CD and EVP-WD models were calibrated using the genetic algorithm (GA) in a three-stage multi-objective calibration workflow, which involved 1) finding the elastic-viscoplastic parameters, 2) finding the damage parameters, and 3) fine-tuning the combined parameters. This procedure was repeated ten times for the EVP-CD and EVP-WD models to investigate the repeatability and robustness of the developed approach. Once calibrated, the semi-empirical models were assessed based on their individual performance at each optimisation stage, as well as their relative performance after the three-stage calibration.

The following section begins by describing how the experimental datasets were processed and separated into calibration and validation subsets (section 4.1). The section continues with an overview of the genetic algorithm (section 4.2) as well as the developed three-stage calibration workflow (section 4.3). The developed calibration workflow is also summarised in the flowchart in Fig. 2.

4.1. Splitting the experimental dataset

In this study, the short-term experimental datasets are used for calibration and the longer-term experimental datasets are used for validation. The experimental data provided by INL includes tests at three temperatures (800°C, 900°C, and 1000°C), with each comprising four creep curves and one tensile curve. At each temperature, the semi-empirical models are calibrated using the two highest stress creep curves and the tensile curve (i.e., short-term data), while validation is performed using the two lowest stress creep curves (i.e., longer-term data). This data selection strategy allows for a demonstration of the models' ability to capture multiple loading configurations, as well as their ability to extrapolate and predict longer-term behaviour using only short-term experimental data.

4.2. Genetic algorithm-based model calibration

The genetic algorithm (GA) is a search technique inspired by the principles of natural selection, and as such, it uses terminology such as

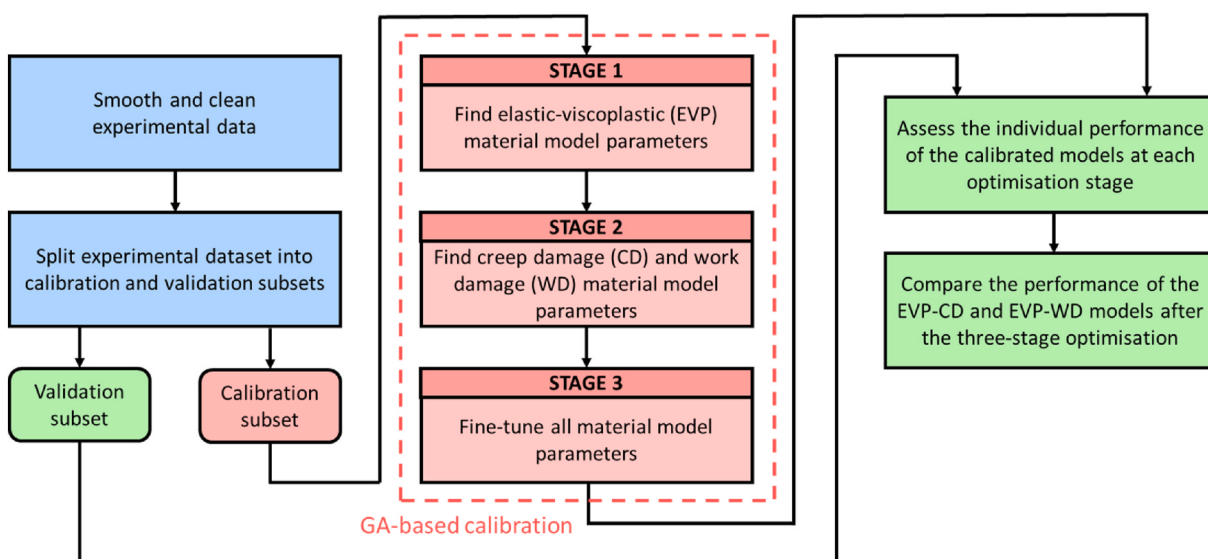


Fig. 2. Flowchart of three-stage multi-objective calibration workflow.

gene, *chromosome*, *population*, *crossover*, and *mutation* [9,23,24]. In the context of using the GA for the calibration of material models, a *gene* represents an unknown material parameter value, a *chromosome* represents a complete set of material parameters, and a *population* represents a collection of chromosomes [10,23]. Parameters such as *crossover probability*, *mutation probability*, *initial population*, and the *number of offspring*, are user-defined hyperparameters governing the behaviour of the GA and, thus, the calibration process. Following Ref. [10,19,22] and through trial and error, the values of these hyperparameters were set to 80%, 1%, 100, and 50, respectively.

In short, the GA begins with an initial population of chromosomes and iteratively evolves the population until it finds a chromosome (i.e., set of material parameters) that best describes the experimentally observed material behaviour based on a defined objective function. The GA was chosen to calibrate the EVP-CD and EVP-WD models (i.e., find the unknown material parameters) due to its integrability to multi-objective optimisation (MOO). This study employs the NSGA-2 implementation of the multi-objective genetic algorithm (MOGA) [47,48] to simultaneously minimise multiple objective functions and capture the material properties from the experimental creep and tensile datasets. The concepts of the GA and MOO are explained in further depth in [Appendix D](#).

In addition to defining the hyperparameters, the bounds for the material parameters of the semi-empirical models were also defined, which affected the shape and size of the parameter space. The bounds were based on literature [43,46,49,50] as well as through trial-and-error. The values used for the lower and upper bounds of the material parameters are summarised in [Appendix B](#). These values were selected such that the parameter space would be small enough for the MOGA to converge in a reasonable amount of time, but large enough to showcase the MOGA's optimisation capabilities [10].

To guide the MOGA in its search for suitable material parameters for the semi-empirical models, objective functions were implemented to minimise the discrepancies between certain material properties extracted from the experimentally observed and simulated creep and tensile curves. These material properties were selected based on their importance in the analysis of engineering systems. The implementations of the objective functions are explained in-depth in [Appendix E](#). To summarise, four objective functions were implemented for the creep curves to minimise discrepancies in the strain values ($E_{\epsilon_{area}}$), minimum creep rate ($E_{\dot{\epsilon}_{min}}$), time-to-failure (E_{t_f}), and strain-to-failure (E_{ϵ_f}). Four additional objective functions were implemented for the tensile curves to minimise discrepancies in the stress values ($E_{\sigma_{area}}$), yield stress (E_{σ_y}), maximum true stress ($E_{\sigma_{MTS}}$), and strain-at-ductility (E_{ϵ_d}). The schematic in [Fig. 3](#) visualises these objective functions on a creep and tensile curve.

After many generations of breeding, the MOGA was terminated with a final population of chromosomes (i.e., sets of material parameter values). After each optimisation run, the average of the defined objectives values was calculated for each chromosome in the final population. The best chromosome (i.e., most optimal set of parameter values) was then identified as the chromosome that has the minimal average of the objective values of the chromosomes in the final population.

4.3. Three-stage calibration

Calibrating the semi-empirical models can be challenging due to their complexity and the high dimensionality of the parameter space. As such, directly optimising the models could incur convergence issues, overfitting, and substantial computational costs. To simplify the calibration process and reduce the computational costs, the optimisation problem was separated into three smaller optimisation stages.

The first optimisation stage (stage 1) involved finding the EVP parameters ($\sigma_{y,0}$, R_{VIIH} , d_{VIIH} , n_{PF} , and η_{PF}) using only the experimental elastic-plastic creep and tensile data. The values of the EVP parameters in the initial population of the MOGA were randomly generated within

their defined bounds. When calibrating the EVP model against creep data, the MOGA optimised with the objective functions for the strain values ($E_{\epsilon_{area}}$) and minimum creep rate ($E_{\dot{\epsilon}_{min}}$) using the creep data up to the minimum creep rate (i.e., onset of tertiary creep). When calibrating against the tensile data, the MOGA optimised with the objective functions for the stress values ($E_{\sigma_{area}}$) and yield stress (E_{σ_y}) using the tensile data up to the maximum true stress. For this stage, the MOGA was terminated after 250 generations.

The second optimisation stage (stage 2) involved fixing the values of the optimised EVP parameters from the first stage (i.e., $\sigma_{y,0}$, R_{VIIH} , d_{VIIH} , n_{PF} , and η_{PF}) before searching for the remaining damage parameters of the semi-empirical models. For the EVP-CD model, the MOGA searched for the A_{CD} , ξ_{CD} , and ϕ_{CD} parameters; and for the EVP-WD model, the MOGA searched for the A_{WD} , a_{WD} , B_{WD} , b_{WD} , α_{WD} , and β_{WD} parameters. The values of the CD and WD parameters in the initial population of the MOGA were, once again, randomly generated within their defined bounds. When calibrating against creep data, the MOGA optimised with the objective functions for the strain values ($E_{\epsilon_{area}}$), minimum creep rate ($E_{\dot{\epsilon}_{min}}$), time-to-failure (E_{t_f}), and strain-to-failure (E_{ϵ_f}). When calibrating against tensile data, the MOGA optimised with the objective functions for the stress values ($E_{\sigma_{area}}$), yield stress (E_{σ_y}), maximum true stress ($E_{\sigma_{MTS}}$), and strain-at-ductility (E_{ϵ_d}). For this stage, the MOGA was terminated after 250 generations for the EVP-CD model, and 500 generations for the EVP-WD model.

The third optimisation stage (stage 3) involved simultaneously fine-tuning the optimised material parameters of the EVP and damage models from the previous optimisation stages. This correctional optimisation aimed to better capture the parameter interactions and resolve any coupling issues between the EVP and damage models. To do this, the initial population of the MOGA was defined with the optimised EVP-CD and EVP-WD parameters from the second optimisation stage. With the initialised parameters, this correctional optimisation was conducted using the same objective functions, calibration data, and number of generations as the second optimisation stage.

5. Results

In an ideal scenario, the calibration of material models should be a straightforward process. However, the complexity of semi-empirical material models – with many unknown material parameters – often complicates this process. A single-stage calibration process, which employs an optimisation algorithm trying to simultaneously find all eight or eleven unknown material parameters, is only applicable in limited cases when calibrating simpler material models [10,16,51] in a relatively tight parameter space. Attempts were made to calibrate EVP-CD and EVP-WD models with a single-stage calibration process against the available experimental creep and tensile datasets. However, the simple single-stage calibration process consistently failed to reliably describe the experimental data due to the many unknown material parameters. It thus became clear that employing a simple single-stage approach is not effective for calibrating advanced models such as EVP-CD and EVP-WD. Hence, the three-stage multi-objective calibration workflow was employed to calibrate the EVP-CD and EVP-WD material models against the INL-provided creep and tensile experimental datasets for Alloy 617 at 800°C, 900°C, and 1000°C. The workflow involved identifying the material parameters of the EVP model and damage (CD, WD) model through two separate optimisations (stages 1 and 2), followed by a correctional optimisation (stage 3) to resolve interdependencies between the two sets of material parameters. The calibration results on the 800°C datasets are shown in the following section, while the results for the 900°C and 1000°C datasets can be found in [Appendix F](#). The developed workflow is also discussed in further depth in section 6.1.

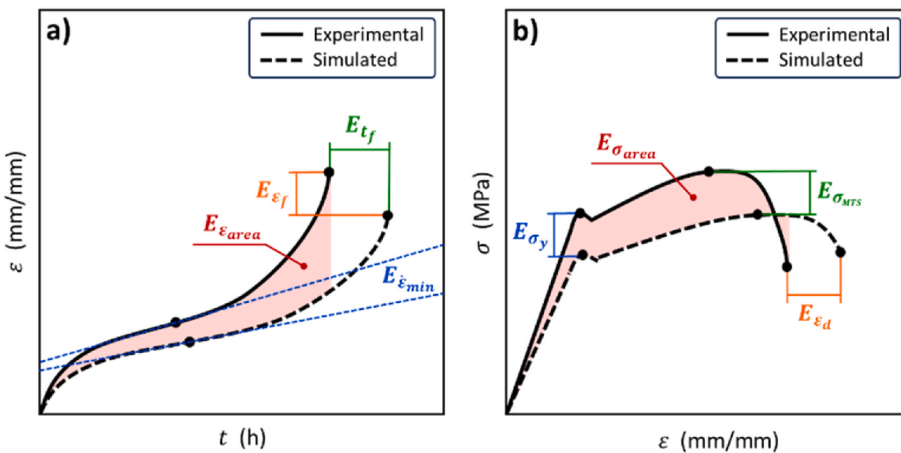


Fig. 3. Schematics of an experimentally observed and simulated a) creep curve and b) tensile curve, annotated with the discrepancies that the implemented objective functions aim to minimise.

5.1. Elastic-viscoplastic – creep damage (EVP-CD) model

Calibrating the EVP-CD model requires finding the five material parameters defining the EVP model ($\sigma_{y,0}$, R_{VH} , d_{VH} , n_{PF} , η_{PF}) and the three parameters defining the CD model (A_{CD} , ξ_{CD} , and ϕ_{CD}). The three-stage calibration process was conducted ten times to find these unknown material parameters. The calibration results for the EVP-CD model at each optimisation stage are shown in Fig. 4, with each plot (a-f) containing the experimental creep and tensile curves (in grey) with the corresponding ten sets of simulated creep and tensile curves (in green or red). To assess the robustness of the developed workflow, the boxplots (g) show the distribution of the found material parameters resulting from the ten independent calibration runs. The material parameters obtained from the best¹ calibration run are shown in Fig. 4g, and the corresponding curves are highlighted with increased opacity in Fig. 4a-f.

The plots in the first column show the results from the initial optimisation (stage 1), where the EVP model was calibrated using the short-term creep curves up to the minimum creep rate ($\dot{\varepsilon}_{min}$) and a tensile curve up to the maximum true stress (σ_{MTS}). It is clear from Fig. 4a that the elastic-plastic creep behaviour was captured accurately and consistently, as demonstrated by the narrow spread of the simulations and their proximity to the experimental data. While the simulated tensile curves in Fig. 4b have a more noticeable spread, the simulations are still of acceptable accuracy. The plots in the second column of Fig. 4 show the results from the second optimisation (stage 2), where the CD model is being calibrated using full creep and tensile curves while the EVP parameters found in the first stage are fixed. The times-to-failure of the creep curves were accurately captured, as shown in Fig. 4c. In particular, the times-to-failure for the longer-term creep curves were predicted exceptionally well, despite them not being used in the calibration process. However, the strains-to-failure were not very accurate, though they are still conservative. While the tensile damage was not captured very well, the EVP-CD model was still able to simulate the strain-at-ductility with reasonable accuracy, as shown in Fig. 4d. The plots in the third column show the results from the correctional optimisation (stage 3), where the EVP and CD parameters were fine-tuned using full creep and tensile curves. As shown in Fig. 4e, the accuracy and consistency of the creep curves were slightly improved in the correctional optimisation, particularly for the strains-to-failure. However, as shown in Fig. 4f, there were no noticeable improvements in the accuracy of the tensile damage, with the strain-at-ductility being worse.

The three-stage optimisation of the EVP-CD model was also conducted using experimental creep and tensile data at 900°C and 1000°C, the results of which can be found in Appendix F. At 900°C, the minimum creep rates and yield stress were accurately captured in the initial optimisation (stage 1). However, the times-to-failure, strains-to-failure, and maximum true stress were not captured very accurately in the second optimisation (stage 2). While the accuracy of the strain-at-ductility improved in the correctional optimisation (stage 3), there were minimal improvements for the other material properties. The short-term creep curves were captured with reasonable accuracy at 1000°C, but the longer-term creep simulations were demonstrably worse, and the tensile failure was poorly predicted.

5.2. Elastic-viscoplastic – work damage (EVP-WD) model

The EVP-WD model is defined by the five material parameters from the EVP model ($\sigma_{y,0}$, R_{VH} , d_{VH} , n_{PF} , η_{PF}) and the six material parameters from the WD model (A_{WD} , a_{WD} , B_{WD} , b_{WD} , α_{WD} , and β_{WD}). As with the EVP-CD model, the three-stage calibration process was conducted ten times to find these unknown material parameters. The calibration results at 800°C are shown in Fig. 5, while the results for the 900°C and 1000°C datasets can be found in Appendix F.

The optimisation results for the EVP-WD model are somewhat consistent with that observed for the EVP-CD model. Specifically, the elastic-plastic behaviour was accurately captured in the initial optimisation (stage 1), and the damage behaviour was captured with less accuracy in the second optimisation (stage 2), particularly for the strains-to-failure for the longer-term creep curves and the strain-at-ductility in the tensile curve. However, the accuracy of the simulations was improved in the correctional optimisation (stage 3), especially for the tensile response. While the EVP-WD model captured the creep behaviour with comparable accuracy to the EVP-CD model, the EVP-WD model was able to capture the tensile behaviour significantly better, specifically regarding the yield stress, maximum true stress, and strain-at-ductility. The improvement from the correctional optimisation (stage 3) was also more significant for the EVP-WD model than for the EVP-CD model.

The three-stage optimisation of the EVP-WD model was also conducted at 900°C and 1000°C, the results of which can also be found in Appendix F. The EVP-WD model was similarly able to outperform the EVP-CD model at 900°C and 1000°C, particularly with the accuracy of the tensile simulations. Notably, the longer-term creep predictions were improved significantly during the correctional optimisation at 900°C. However, the EVP-WD model struggled to accurately capture and predict the creep behaviour at 1000°C.

¹ The 'best' of the ten independent calibration runs were identified based on the minimality of the averaged objective values after the final optimisation stage (see section 4.2).

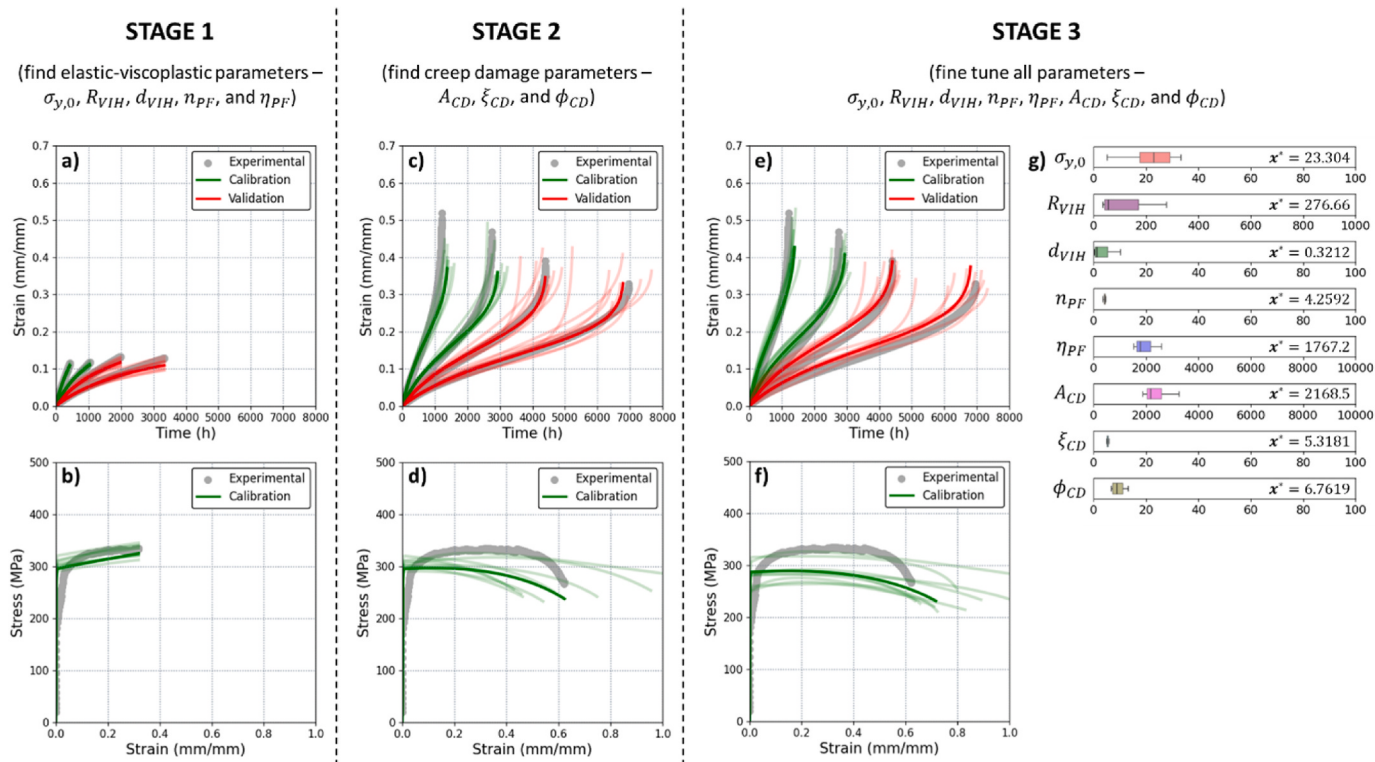


Fig. 4. Optimisation results for the EVP-CD model at 800°C, calibrated with short-term creep curves (70MPa and 80MPa) and tensile curve, and validated with longer-term creep curves (60MPa and 65MPa). The top row of plots (a, c, e) shows the creep results while the bottom row of plots (b, d, and f) shows the tensile results after stages 1, 2, and 3. The experimental datasets are in grey, the simulated curves used for calibration are in green, and the simulated curves used for validation are in red. The boxplots (g) show the distribution of the found parameters, where x^* represents the optimal parameter value, the vertical line represents the mean, the boxes represent the standard deviations, and the whiskers represent the ranges. (For interpretation of the references to colour in this figure legend, the reader is referred to the Web version of this article.)

6. Discussion

The following section provides a discussion of the developed three-stage multi-objective calibration process (section 6.1), an assessment of the calibrated EVP-CD and EVP-WD models (section 6.2), as well as an overview of the computational resources required to calibrate these semi-empirical models (section 6.3).

6.1. Calibration process

Preliminary trials were undertaken to simultaneously search for all the parameters of the EVP-CD and EVP-WD models in a single optimisation stage. However, the calibrations were computationally expensive and consistently failed. Hence, a modular approach was undertaken to calibrate the models in three separate stages. In the initial optimisation (stage 1, shown in Fig. 4a-b and Fig. 5a-b), the EVP model accurately captured the elastic-plastic behaviour of the experimental creep and tensile data. In the subsequent optimisation (stage 2, shown in Fig. 4c-d and Fig. 5c-d), the coupled EVP-CD and EVP-WD models were not very accurate in capturing damage behaviour, particularly for the strains-to-failure. Specifically, for the best calibration run at 800°C, the average relative errors of the strains-to-failure for the EVP-CD and EVP-WD models were 16% and 18%, respectively. These inaccuracies could be attributed to the limitations of the infinitesimal strain theory, which disregards the effects of large deformations, rotations, and nonlinear material behaviour. Additionally, the modular approach of the separate optimisations simplified and reduced the computational burden of the calibration process, by splitting the high-dimensional parameter space into two lower-dimensional parameter spaces. However, separate optimisations can overlook the interactions between the viscoplastic response and damage accumulation – such as the effects of localised

plastic deformation on damage initiation and growth rates, and the effects of damage evolution on the strain rate sensitivity, creep deformation rate, and strain hardening behaviour. The neglect of these interactions combined with the limitations of the infinitesimal strain theory likely contributed to the decreased accuracy in capturing the damage behaviour during the second optimisation.

The correctional optimisation (stage 3, shown in Fig. 4e-f and Fig. 5e-f) aimed to better capture the parameter interactions by simultaneously fine-tuning the parameters of the EVP and damage (CD, WD) models. The overall accuracy of both models improved in the correctional optimisation – for instance, for the best calibration run at 800°C, the averaged objective values for the EVP-CD and EVP-WD models decreased by 14% and 27%, respectively. Notably, the EVP-WD model showed more substantial improvements, which was attributed to the larger number of material parameters in the WD model as well as the tighter coupling between the EVP and WD models, particularly with the WD model's reliance on the loading history and accumulated work. While initialising the parameters helped reduce the computational burden by allowing for faster convergence, the effectiveness of the correctional optimisation still hinges on the assumption that the separately optimised parameters are close to their optimal values. This can be problematic for more complex models (e.g., physics-based models), where the correctional optimisation could further worsen the simulations by overfitting the calibration datasets.

The boxplots in Fig. 4g and Fig. 5g show the optimised parameters after the three-stage calibration runs. During these runs, the MOGA converged towards a spread of different parameter values. This lack of uniqueness in the optimised parameters is attributed to the non-deterministic nature of the GA, the non-linearity of the objective functions, the predefined termination of the MOGA (after 250 or 500 generations), as well as the optimisation problem not being sufficiently

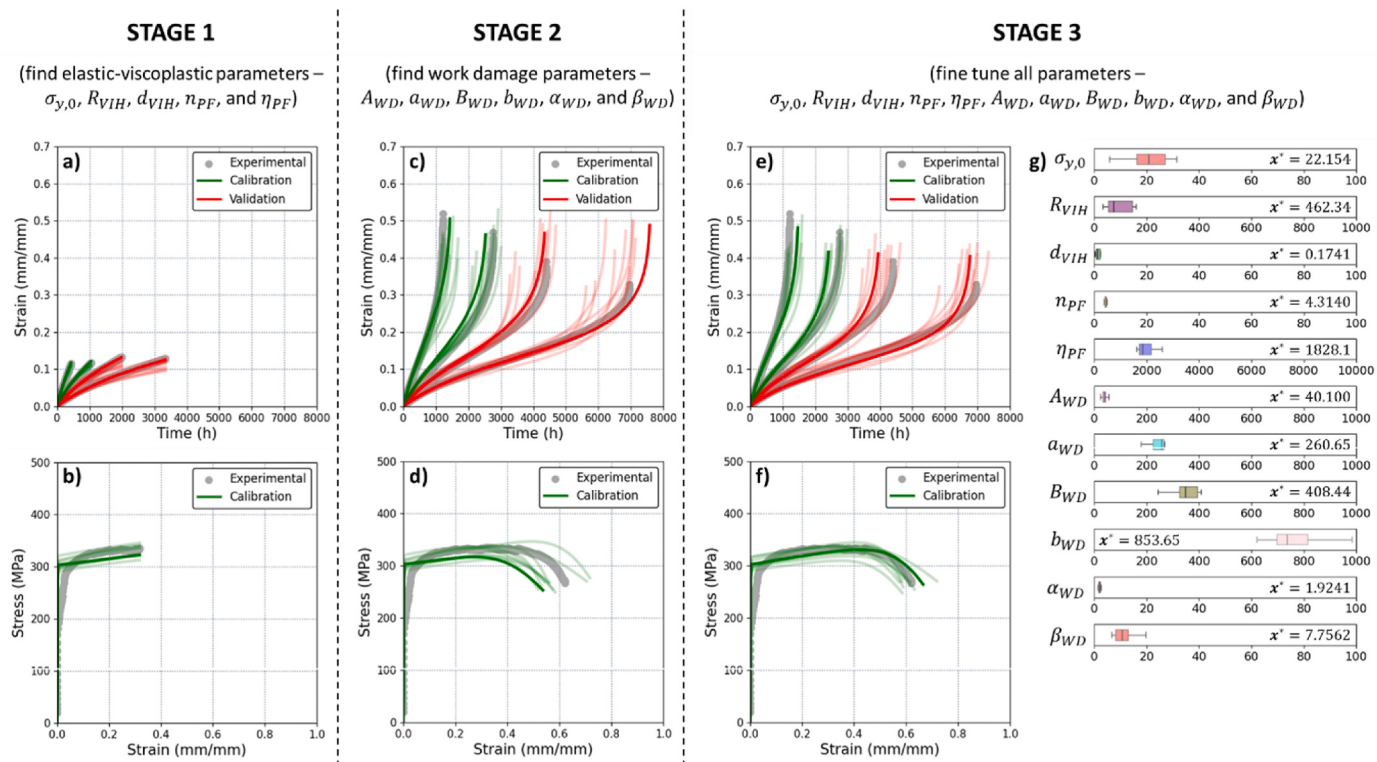


Fig. 5. Optimisation results for the EVP-WD model at 800°C, calibrated with short-term creep curves (70MPa and 80MPa) and tensile curve, and validated with longer-term creep curves (60MPa and 65MPa). The top row of plots (a, c, e) shows the creep results while the bottom row of plots (b, d, and f) shows the tensile results after stages 1, 2, and 3. The experimental datasets are in grey, the simulated curves used for calibration are in green, and the simulated curves used for validation are in red. The boxplots (g) show the distribution of the found parameters, where x^* represents the optimal parameter value, the vertical line represents the mean, the boxes represent the standard deviations, and the whiskers represent the ranges. (For interpretation of the references to colour in this figure legend, the reader is referred to the Web version of this article.)

constrained. The spread could potentially be reduced by introducing additional calibration datasets, reducing the size of the searched parameter space, and further tuning the MOGA's hyperparameters. That said, the spread of the parameters was relatively narrow compared to the applied bounds, which demonstrates the repeatability of the calibration process and the sufficiency of the current setup for optimising the EVP-CD and EVP-WD models. The boxplots in Fig. 5g also show that there were inconsistencies between the optimised values for the A_{WD} , a_{WD} , B_{WD} , and b_{WD} parameters and the experimentally observed values discussed in section 3.3. These inconsistencies were due to the optimised values being based at one temperature, while the experimentally observed values were calculated from all three temperatures. It is worth noting that attempts were made to fix these parameters, which did not yield models that predicted the data well. However, the optimised values are still of the same order of magnitude, which suggests that the experimentally observed parameter values should only be used to determine the bounds of the parameters for the calibration process.

The robustness of the three-stage multi-objective calibration workflow depends on the underlying microstructural stability of the material. The success of the calibration workflow in capturing the behaviour of Alloy 617 can be attributed to its high microstructural stability, which minimises phase transformations and limits the influence of thermodynamic effects on deformation [52]. However, materials that are prone to phase changes, carbide coarsening, or grain boundary evolution, can undergo significant microstructural changes over prolonged high-temperature loading. These changes can trigger shifts in the dominant deformation and degradation mechanisms, which in turn alter the material's mechanical response [53–55]. For these microstructurally unstable materials, the mechanical response captured during stage 1 (initial yielding) and stage 2 (damage progression) may reflect drastically different microstructural states. This can cause the correctional

optimisation to over-fit either the yielding or damage response, rather than achieving a balanced fit across the entire deformation history. To address this issue, the calibration workflow can be extended with additional stages spaced across narrower intervals, allowing the parameter subsets to adapt progressively to the material's evolving behaviour.

6.2. Performance of models

As discussed in section 3.1, the semi-empirical models were formulated within the infinitesimal strain framework [38–40] despite the experimental data exceeding the framework's validity limit. Consequently, these models were empirically calibrated to reproduce the relevant macroscopic behaviours observed in tensile and creep tests. In this sense, the EVP-CD and EVP-WD models are suitable for fitness-for-service assessments where deformation paths remain within the calibrated range.

To evaluate the predictive capabilities of the fully calibrated EVP-CD and EVP-WD models (i.e., after stage 3), a detailed comparison was performed between experimentally observed and simulated material properties under creep and tensile loading at 800°C, 900°C, and 1000°C. The comparisons for the best calibration run are shown in Fig. 6 with the plots in the top row (a, b, c, and d) comparing the total creep deformation (ϵ_{area}), minimum creep rate ($\dot{\epsilon}_{min}$), time-to-failure (t_f), and strain-to-failure (ϵ_f) for the creep curves, and the plots in the bottom row (e, f, g, and h) comparing the toughness (σ_{area}), yield stress (σ_y), maximum true stress (σ_{MTS}), and strain-at-ductility (ϵ_d) for the tensile curves. These plotted material properties correspond to the objective functions used for the MOGA optimisation, as described in section 4.2, and the accuracies in capturing the material properties are indicated by the proximity of the individual symbols to the ideal 1:1 line.

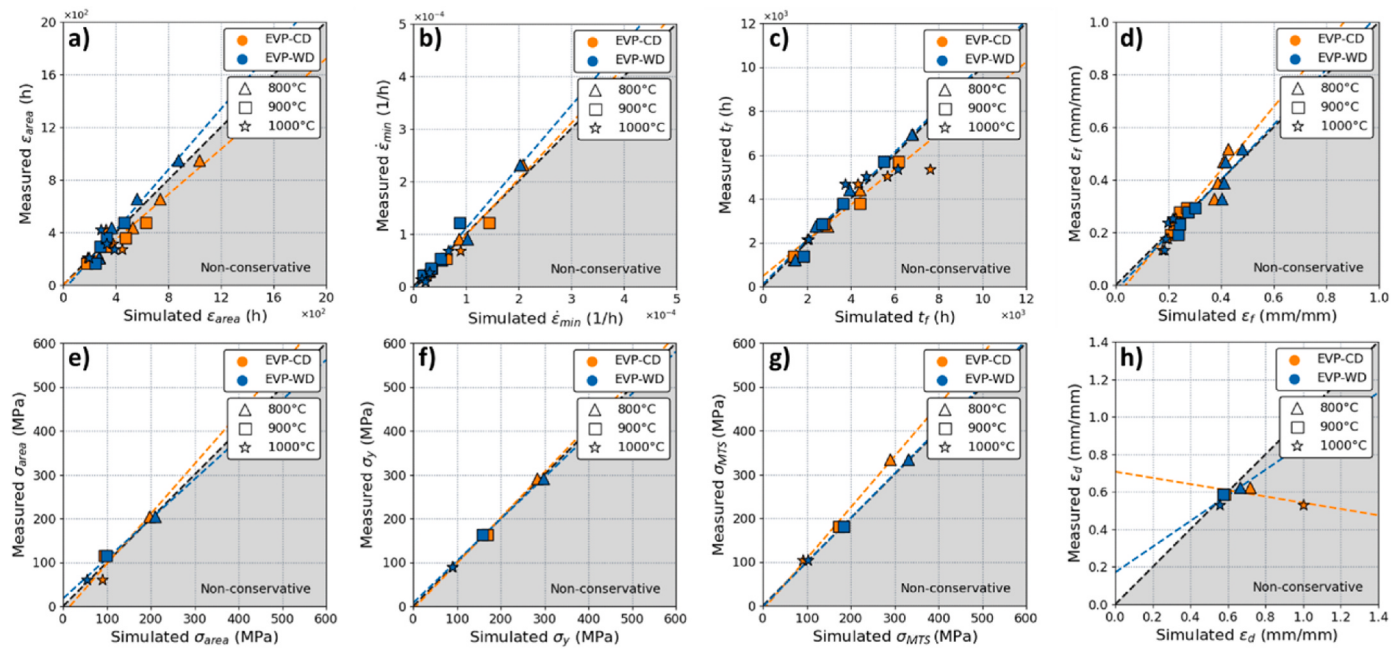


Fig. 6. Assessment of simulated material properties by the EVP-CD model (orange) and EVP-WD model (blue) at 800 °C, 900 °C, and 1000 °C. The plots in a), b), c), and d) compare the total creep deformation, minimum creep rate, time-to-failure, and strain-to-failure of the experimental and simulated creep curves. The plots in e), f), g), and h) compare the toughness, yield stress, maximum tensile stress, and strain-at-ductility of the experimental and simulated tensile curves. (For interpretation of the references to colour in this figure legend, the reader is referred to the Web version of this article.)

As seen in Fig. 6, the EVP-CD and EVP-WD models capture the creep behaviour of Alloy 617 with comparable accuracy, with the EVP-WD model slightly outperforming for the times- and strains-to-failure. In addition, most of the material properties captured by the EVP-WD model are conservative, which is useful for capturing the safe lifetimes of materials under in-service operating conditions. Both models were able to accurately predict the longer-term creep curves (i.e., validation data), which showcase their capacity to encapsulate the physical processes inherent to the material. These results also demonstrate that short-term experimental data can sufficiently calibrate the EVP-CD and EVP-WD model to predict longer-term behaviour, which is significant since short-term data is easier and less costly to obtain than longer-term experimental data. However, in this study, the longer-term validation data only captures times-to-failure out to around one year, while VHTR designs will require 100,000 h or more of component lifetime. Thus, future work will be required to understand if accurate extrapolations can be made out to 100,000h, and if so, what times-to-failure would be required for the calibration data. Additionally, the accuracy of the time-to-failure predictions is shown to decrease with increasing temperature (Fig. 6c). This was attributed to the increasing effect of the in-air oxidation during the creep testing [33–35] at higher temperatures (i.e., 1000°C), which the models and the data removal (described in section 2) were unable to account for. That said, reduced time-to-failure accuracy at 1000°C is not a concern for VHTR designs using ASME Code Case N-898, which limits the temperature to 954°C and below.

When it comes to tensile behaviour, both models accurately captured the yield stress and toughness. This is expected since both models share the EVP model, which is mostly responsible for capturing those material properties. The greatest discrepancies in the performance of the two models lie in the capturing of the maximum true stress and strain-at-ductility. This is demonstrated in Fig. 6g-h, with the EVP-WD model substantially outperforming the EVP-CD model. These discrepancies can be attributed to the fact that the CD model posits that damage accumulates as a function of time instead of strain or plastic work density [45]. As such, the CD model is not mathematically suited to capture failure in tensile deformation, especially at the comparatively high strain rates of the tensile data (i.e., $1.0 \times 10^{-4} \text{ s}^{-1}$). However, the WD

model defines the damage accumulation using piecewise correlations that simulate separate behaviours depending on the plastic work density rate, allowing the WD model to account for the contrastingly different strain rates observed in creep and tensile experiments. These results suggest that the WD model could be extended to capture additional loading configurations (e.g., fatigue data) by defining the critical plastic work density (W_{crit}) with an N-linear function and the damage exponent (n_d) with an N-step function, where N refers to the number of loading configurations to be captured.

6.3. Computational resources

While the EVP-WD model can capture tensile damage with greater accuracy compared to the EVP-CD model, the EVP-WD model suffers from a more complex implementation, larger number of material parameters, and higher evaluation times. Specifically, each evaluation of the EVP-WD model took an average of 1.395s of CPU time on a single core of a 3.80 GHz Intel Core i7-10700KF processor, while each evaluation of the EVP-CD model took an average of only 0.595s. The EVP-WD model was also found to require more generations (500) to reach a suitable set of material parameter values compared to the EVP-CD model (250). This was attributed to the larger parameter space as well as the tighter coupling between the EVP and WD models. As such, with the higher evaluation time and number of generations, the EVP-WD model requires significantly more computational resources to calibrate.

7. Conclusion

In this study, we demonstrate a three-stage calibration framework developed for the simultaneous calibration of semi-empirical material models to capture the high-temperature creep and tensile behaviour of structural alloys. The framework was applied to Alloy 617 at 800 °C, 900 °C, and 1000 °C, though it is equally applicable to other high-temperature alloys. The models employed a temperature-dependent elastic-viscoplastic (EVP) formulation coupled with either classical creep damage (EVP-CD) or work-based damage (EVP-WD). A multi-objective genetic algorithm (MOGA) was utilised to concurrently fit

both model variants to short-term creep and tensile datasets provided by Idaho National Laboratory (INL). Validation was subsequently performed against independent longer-term creep measurements, allowing assessment of the models' predictive capabilities beyond the calibration dataset.

The three-stage calibration consisted of: (1) identification of EVP parameters, (2) calibration of damage parameters (CD or WD), and (3) joint fine-tuning of all parameters. This staged approach enabled robust and efficient calibration against the short-term experimental data. The repeatability of the calibration was assessed through ten independent optimisation runs, revealing some variability due to the stochastic nature of the genetic algorithm and the inherent non-linearity of the calibration problem. It is therefore recommended to perform multiple calibration runs to ensure the identification of robust and representative set of material parameters.

Once calibrated, both EVP-CD and EVP-WD models successfully captured the creep response of Alloy 617 at 800°C and 900°C with comparable accuracy. However, predictive performance decreased at 1000°C due to surface oxidation effects leading to atypical tertiary creep behaviour, which the current models were not formulated to describe. Overall, the EVP-WD model demonstrated superior accuracy in reproducing the full tensile stress-strain response compared to the EVP-CD model, although at the cost of increased computational complexity and calibration effort. Additionally, the WD formulation, by capturing deformation history through plastic work density, holds potential for extension to other loading scenarios.

It is important to acknowledge that the constitutive models employed here were based on infinitesimal strain theory, thus their accuracy at large deformations – such as those near tensile failure – may be limited. Nevertheless, they remain practically applicable and reliable for moderate strains, typical of creep deformation and inelastic service

conditions. The developed three-stage calibration workflow addresses the significant challenge of simultaneously calibrating material models to distinct mechanical responses, offering a structured foundation for extending this approach to alternative constitutive frameworks or different material systems.

CRediT authorship contribution statement

J. Choi: Writing – review & editing, Writing – original draft, Visualization, Software, Formal analysis, Data curation. **O. Muránsky:** Writing – review & editing, Writing – original draft, Supervision, Resources, Conceptualization. **M.C. Messner:** Writing – review & editing, Supervision, Software, Funding acquisition, Conceptualization. **J.J. Kružic:** Writing – review & editing, Supervision, Funding acquisition. **M.D. McMurtrey:** Writing – review & editing, Data curation.

Declaration of competing interest

The authors declare that they have no known competing financial interests or personal relationships that could have appeared to influence the work reported in this paper.

Acknowledgements

The authors acknowledge the support, funding, and resources from the NSW government as well as ANSTO, through their Future Now scholarship program. The contributions of these two organisations have been invaluable in the successful completion of this study. The work of MCM was sponsored by the U.S. Department of Energy, under Contract No. DE-AC02-06CH11357 with Argonne National Laboratory, managed and operated by UChicago Argonne LLC.

Appendix A

In this study, experimental creep and tensile data of Alloy 617 was provided by INL [27] to support the calibration and validation of the semi-empirical models. A summary of the experimental creep data is presented in [Table A1](#), where T represents the temperature, σ represents the applied stress, and $\dot{\epsilon}_{min}$ represents the minimum creep rate. In addition, ϵ_f and t_f represent the true, experimentally measured strain- and time-to-failure, whereas $\epsilon_{f,o}$ and $t_{f,o}$ represent the strain and time at which the oxidation-induced atypical tertiary behaviour was removed. The $\epsilon_{f,o}$ and $t_{f,o}$ values were thus only defined for the oxidation-affected creep curves.

Table A1

Summary of experimental creep data of Alloy 617 from Idaho National Laboratory.

Sample	Time scale	T (°C)	σ (MPa)	$\dot{\epsilon}_{min}$ ($10^{-5}/\text{h}$)	ϵ_f (mm/mm)	$\epsilon_{f,o}$ (mm/mm)	t_f (h)	$t_{f,o}$ (h)
G32	Longer-term	800	60	2.89	0.328	–	6949.7	–
G33	Longer-term	800	65	5.04	0.390	–	4404.1	–
G44	Short-term	800	70	9.03	0.468	–	2750.7	–
G25	Short-term	800	80	23.3	0.518	–	1208.1	–
G59	Longer-term	900	26	2.19	0.349	0.193	7983.8	5706.1
G45	Longer-term	900	28	3.53	0.231	–	3781.8	–
G50	Short-term	900	31	5.37	0.277	–	2846.1	–
G22	Short-term	900	36	12.2	0.293	–	1380.4	–
G39	Longer-term	1000	11	1.29	0.565	0.139	18923	5404.8
G48	Longer-term	1000	12	0.990	0.641	0.177	16696	5026.9
G30	Short-term	1000	13	2.66	0.535	0.239	8768.1	4688.3
G18	Short-term	1000	16	6.76	0.462	0.255	3034.1	2154.6

A summary of the experimental tensile data is presented in [Table A2](#), where $\dot{\epsilon}$ represents the strain rate, σ_y represents the yield strength, σ_{UTS} represents the ultimate tensile stress, σ_{MTS} represents the maximum true stress, σ_d represents the stress-at-ductility, and ϵ_d represents the strain-at-ductility. Note that the values for $\dot{\epsilon}$, ϵ_f , σ_y , and σ_{UTS} are reported in terms of engineering stress and strain, while the values for σ_{MTS} , σ_d , and ϵ_d are reported in terms of true stress and strain.

Table A2

Summary of experimental tensile data of Alloy 617 from Idaho National Laboratory.

Sample	Time scale	T (°C)	$\dot{\epsilon}$ (10 ⁻⁴ /h)	ϵ_f (mm/mm)	σ_y (MPa)	σ_{UTS} (MPa)	σ_{MTS} (MPa)	σ_d (MPa)	ϵ_d (mm/mm)
D7	Short-term	800	1.04	0.940	189	289.5	334.3	267.0	0.622
D10	Short-term	900	1.00	1.033	163	166.2	180.7	144.4	0.587
D12	Short-term	1000	1.03	0.987	90	123.6	104.6	83.6	0.527

Appendix B

Table B1 summarises the material parameters for the EVP, EVP-CD, and EVP-WD models. The table also contains information about the lower and upper bounds set for each material parameter during the MOGA optimisations.

Table B1

Summary of material parameters for EVP, EVP-CD, and EVP-WD models.

Material Model	Parameter	Symbol	Lower Bound	Upper Bound	Units
Elastic-viscoplastic (EVP)	Initial yield stress	$\sigma_{y,0}$	0.0	100	MPa
	Isotropic hardening stress	R_{VH}	0.0	1000	MPa
	Isotropic hardening modulus	d_{VH}	0.0	100	—
	Flow surface exponent	n_{PF}	0.0	100	—
	Viscoplastic fluidity	η_{PF}	0.0	10000	MPa
Creep damage (CD)	Stress prefactor	A_{CD}	0.0	10000	MPa
	Stress power law exponent	ξ_{CD}	0.0	100	—
	Damage power law exponent	ϕ_{CD}	0.0	100	—
Work damage (WD)	Creep critical work gradient	A_{WD}	0.0	1000	s
	Creep critical work intercept	a_{WD}	0.0	1000	MPa/s
	Tensile critical work gradient	B_{WD}	0.0	1000	s
	Tensile critical work intercept	b_{WD}	0.0	1000	MPa/s
	Creep damage exponent	α_{WD}	0.0	100	—
	Tensile damage exponent	β_{WD}	0.0	100	—

Appendix C

The critical plastic work density (W_{crit}) describes the minimum amount of work required to initiate dislocation movement in a material, while the plastic work density rate (\dot{W}) is the rate at which energy is expended during plastic deformation. The respective definitions for the critical work density and work density rate are shown in Eqs. (10) and (11), where σ represents stress, ϵ represents strain, and ϵ_f represents the strain-to-failure.

$$W_{crit} = \int_0^{\epsilon_f} \sigma : d\epsilon_{vp} \quad (10)$$

$$\dot{W} = \sigma : \dot{\epsilon}_{vp} \quad (11)$$

The critical work density function is based on the relationship between the critical work density and average work density rate in the INL-provided experimental creep and tensile data of Alloy 617. After removing the effects of oxidation from the affected creep curves (see section 2), the critical work density was plotted against the average work density rate of the experimental data, as shown in Fig. C1. The data points in Fig. C1 suggest independent linear relationships between the critical work density and the logarithmic average work density rate for the creep and tensile data. Notably, the tensile line of best fit is shown to have a higher gradient and higher intercept than the creep line of best fit.

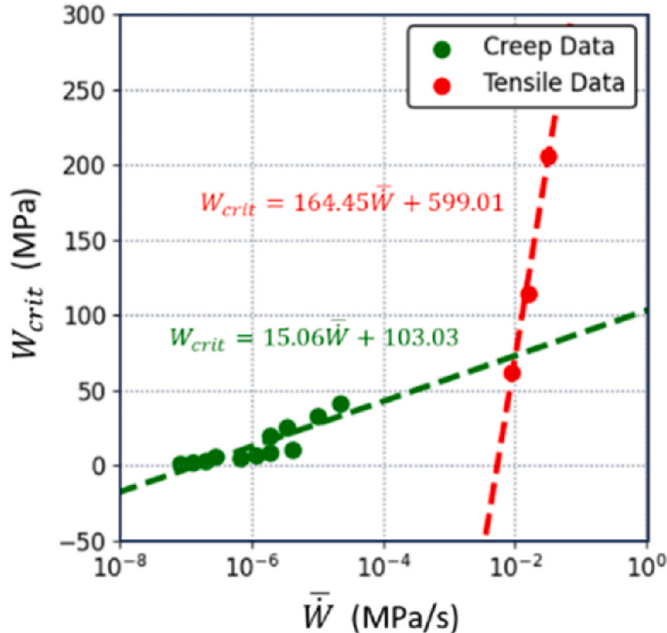


Fig. C1. Critical plastic work density and logarithmic average plastic work density rate of experimental creep and tensile data of Alloy 617; the creep relationship is represented in green, and the tensile relationship is represented in red.

To simulate the experimentally observed relationship in Fig. C1, the critical work density is defined as a bilinear function. The definition is shown in Eqs. (12)–(14), where A_{WD} and a_{WD} define the linear relationship for creep behaviour and B_{WD} and b_{WD} define the linear relationship for tensile behaviour. The λ_1 term represents the work density rate threshold where the critical work density begins to asymptotically approach zero, and the λ_2 term represents the intersection of the creep line and tensile line. Note that the exponential decay term (when $\log_{10}(\dot{W}) < \lambda_1$) was introduced to ensure that $W_{crit} \rightarrow 0$ as $\dot{W} \rightarrow 0$.

$$W_{crit} = \begin{cases} A_{WD} e^{\log_{10}(\dot{W}) - \lambda_1}, \log_{10}(\dot{W}) < \lambda_1 \\ A_{WD} \log_{10}(\dot{W}) + a_{WD}, \lambda_1 \leq \log_{10}(\dot{W}) < \lambda_2 \\ B_{WD} \log_{10}(\dot{W}) + b_{WD}, \lambda_2 \leq \log_{10}(\dot{W}) \end{cases} \quad (12)$$

$$\lambda_1 = 1.0 - a_{WD}/A_{WD} \quad (13)$$

$$\lambda_2 = \frac{b_{WD} - a_{WD}}{A_{WD} - B_{WD}} \quad (14)$$

The damage exponent (n_d) is defined as a step function of the work density rate (\dot{W}), such that the value of the damage exponent is dependent on the loading configuration (i.e., creep or tensile). The damage exponent function is defined in Eqs. (15) and (16), where α_{WD} represents the creep damage exponent, β_{WD} represents the tensile damage exponent, and δ represents a sinusoidal function that smoothly transitions between the α_{WD} and β_{WD} values. Additionally, γ represents some small value that controls the speed of the transition; in this study, γ is set to 0.5.

$$n_d = \begin{cases} \alpha_{WD}, \log_{10}(\dot{W}) < \lambda_2 - \gamma \\ \delta, \lambda_2 - \gamma \leq \log_{10}(\dot{W}) < \lambda_2 + \gamma \\ \beta_{WD}, \lambda_2 + \gamma \leq \log_{10}(\dot{W}) \end{cases} \quad (15)$$

$$\delta = \frac{\beta_{WD} - \alpha_{WD}}{2} \cdot \sin\left(\frac{\pi}{2\gamma} (\log_{10}(\dot{W}) - \lambda_2)\right) + \frac{\alpha_{WD} + \beta_{WD}}{2} \quad (16)$$

Schematics illustrating the critical work density (W_{crit}) function and the damage exponent (n_d) function are shown in Fig. C2.

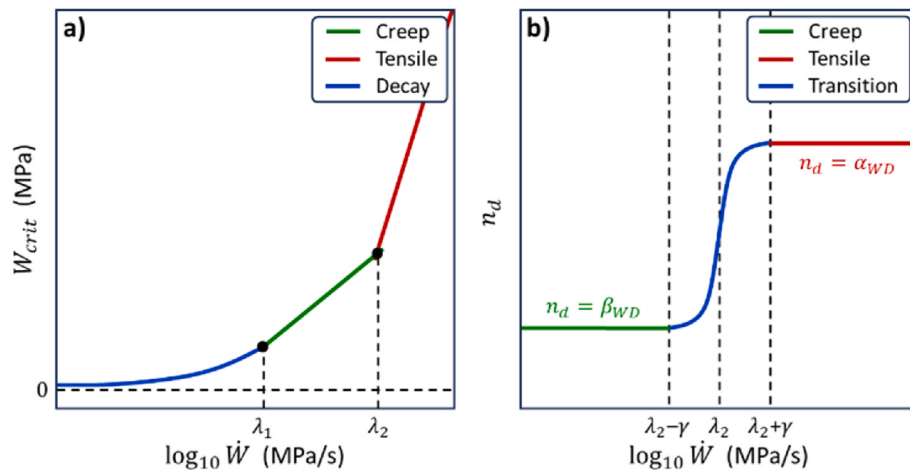


Fig. C2. Schematics of a) critical plastic work density and the b) damage exponent the piecewise functions.

Appendix D

The genetic algorithm (GA) is a randomised search technique within the wider spectrum of evolutionary algorithms, inspired by the principles of biological evolution and natural selection [10]. To calibrate a material model, the GA will use an objective function to assess how well the calibrated model can capture the experimentally observed material response. This objective function describes the discrepancies between the experimental data and the simulated response from the calibrated model. An optimal set of material parameters would thus correspond to the minimal value evaluated by the objective function (i.e., the minimal objective value). The aim of the GA is to produce a population of the fittest chromosomes, where the fitness of a chromosome corresponds to the minimality of the objective value.

To achieve this aim, the GA begins with an initial population of chromosomes with randomly generated genes. Every generation, the GA evaluates the fitness of all the chromosomes in the population and selects the fittest chromosomes to mate and pass on their genetic information to their offspring. The mating of two chromosomes involves the crossover and mutation operators. The crossover operator selects a subset of genes from each chromosome and combines them to produce an offspring chromosome that inherits the combined genes. Doing so promotes the exchange of information between the parent chromosomes, potentially creating offspring with improved fitness. The mutation operator applies small random changes to one or more genes in the offspring, which promotes diversity as the population evolves to prevent premature convergence to suboptimal solutions [10,19]. Together, these operators help the GA explore the parameter space, escape local minima, and converge towards the global minima [10,19]. The crossover and mutation operators activate at user-defined probabilities for each chromosome. If these probabilities are configured correctly, the GA will eventually terminate with a population that contains a quasi-optimal chromosome (i.e., set of parameters) that corresponds to a quasi-minimal objective value [10].

The GA relies on an objective function to minimise the discrepancy between the experimentally observed material response and the simulated response from the calibrated model. Depending on the loading configuration, the material response could comprise multiple distinct material properties, with each material property serving as a source of discrepancy. These discrepancies are minimised to accurately capture the material response, which can be challenging for the traditional GA, since it only considers a single objective function. A typical solution is to combine the multiple discrepancies into a weighted objective function. However, selecting a suitable equation and appropriate weight values may unnecessarily complicate an already complex optimisation problem. To address this, separate objective functions are defined for each material distinct property, with multi-objective optimisation (MOO) being used to simultaneously minimise the multiple objective functions.

The goal of an MOO problem is to find the solution (i.e., set of parameter values) that corresponds to the minimal objective values. In MOO, a solution is considered Pareto efficient if none of the objective values can be reduced without increasing the other objective values [48]. The Pareto front describes the set of all the Pareto efficient solutions. The optimiser can distinguish the optimal solution from the other solutions in the Pareto front based on subjective preference information [48]. The multi-objective genetic algorithm (MOGA) combines the concepts of the GA and MOO, with a popular example being the non-dominated sorting genetic algorithm-II (NSGA-II) [47]. Since GAs are population-based, they are advantageous for MOO in that they can approximate the entire Pareto front every generation.

Appendix E

The following discusses the implementations of the four creep objective functions and four tensile objective functions used in the MOGA optimisations. Note that N represents the number of experimental curves used to calibrate the model. As discussed in section 4.1, the semi-empirical models are calibrated with short-term experimental data, which comprises two low-stress creep curves and one tensile curve for each temperature. As such, the creep objective functions set $N = 2$ while the tensile objective functions set $N = 1$.

The strain objective function ($E_{\varepsilon_{area}}$) minimises the common area between the experimental and simulated creep curves, by assessing the strain values of the creep curves at evenly spaced time intervals. The objective function is defined in Eq. (17), where M represents the number of assessed values, $\tilde{\varepsilon}$ represents an experimental strain value, $\hat{\varepsilon}$ represents a simulated strain value, and $\bar{\tilde{\varepsilon}}$ represents the average of the experimental strain values. In this study, M is set to 50 to obtain a sufficient approximation of the area while reducing the number of evaluations. Note that the $\bar{\tilde{\varepsilon}}$ term is used instead of the $\tilde{\varepsilon}$ term to prevent the relative errors of the small experimental strain values from dominating the objective value.

$$E_{\epsilon_{area}} = \frac{1}{NM} \sum_{i=1}^N \sum_{j=1}^M \left(\frac{(\tilde{\epsilon})_{ij} - (\hat{\epsilon})_{ij}}{(\bar{\epsilon})_i} \right)^2 \quad (17)$$

The minimum creep rate objective function ($E_{\dot{\epsilon}_{min}}$) minimises the discrepancy between the steady-state gradient of the experimental and simulated creep curves. The objective function is defined in Eq. (18), where $\tilde{\dot{\epsilon}}_{min}$ represents the experimental minimum creep rate and $\hat{\dot{\epsilon}}_{min}$ represents the simulated minimum creep rate.

$$E_{\dot{\epsilon}_{min}} = \frac{1}{N} \sum_{i=1}^N \left(\frac{(\tilde{\dot{\epsilon}}_{min})_i - (\hat{\dot{\epsilon}}_{min})_i}{(\tilde{\dot{\epsilon}}_{min})_i} \right)^2 \quad (18)$$

The time-to-failure objective function (E_{t_f}) minimises the horizontal distance between the endpoints of the experimental and simulated creep curves. The objective function is defined in Eq. (19), where \tilde{t}_f represents the experimental time-to-failure and \hat{t}_f represents the simulated time-to-failure.

$$E_{t_f} = \frac{1}{N} \sum_{i=1}^N \left(\frac{(\tilde{t}_f)_i - (\hat{t}_f)_i}{(\tilde{t}_f)_i} \right)^2 \quad (19)$$

The strain-to-failure objective function (E_{ϵ_f}) minimises the vertical distance between the endpoints of the experimental and simulated creep curves. The objective function is defined in Eq. (20), where $\tilde{\epsilon}_f$ represents the experimental strain-to-failure and $\hat{\epsilon}_f$ represents the simulated strain-to-failure.

$$E_{\epsilon_f} = \frac{1}{N} \sum_{i=1}^N \left(\frac{(\tilde{\epsilon}_f)_i - (\hat{\epsilon}_f)_i}{(\tilde{\epsilon}_f)_i} \right)^2 \quad (20)$$

The stress objective function ($E_{\sigma_{area}}$) minimises the common area between the experimental and simulated tensile curves, by assessing the stress values of the tensile curves at evenly spaced strain intervals. The objective function is defined in Eq. (21), where $\tilde{\sigma}$ represents an experimental stress value, $\hat{\sigma}$ represents a simulated stress value, and $\bar{\sigma}$ represents the average of the experimental stress values.

$$E_{\sigma_{area}} = \frac{1}{NM} \sum_{i=1}^N \sum_{j=1}^M \left(\frac{(\tilde{\sigma})_{ij} - (\hat{\sigma})_{ij}}{(\bar{\sigma})_i} \right)^2 \quad (21)$$

The yield stress objective function (E_{σ_y}) minimises the discrepancy between the yield stress of the experimental and simulated tensile curves. The objective function is defined in Eq. (22), where $\tilde{\sigma}_y$ represents the experimental yield stress and $\hat{\sigma}_y$ represents the simulated yield stress.

$$E_{\sigma_y} = \frac{1}{N} \sum_{i=1}^N \left(\frac{(\tilde{\sigma}_y)_i - (\hat{\sigma}_y)_i}{(\tilde{\sigma}_y)_i} \right)^2 \quad (22)$$

The maximum true stress objective function ($E_{\sigma_{MTS}}$) minimises the discrepancy between the maximum true stress of the experimental and simulated tensile curves. The objective function is defined in Eq. (23), where $\tilde{\sigma}_{MTS}$ represents the experimental maximum true stress and $\hat{\sigma}_{MTS}$ represents the simulated maximum true stress.

$$E_{\sigma_{MTS}} = \frac{1}{N} \sum_{i=1}^N \left(\frac{(\tilde{\sigma}_{MTS})_i - (\hat{\sigma}_{MTS})_i}{(\tilde{\sigma}_{MTS})_i} \right)^2 \quad (23)$$

Finally, the strain-at-ductility objective function (E_{ϵ_d}) minimises the horizontal distance between the endpoints of the experimental and simulated tensile curves. The objective function is defined in Eq. (24), where $\tilde{\epsilon}_d$ represents the experimental strain-at-ductility and $\hat{\epsilon}_d$ represents the simulated strain-at-ductility.

$$E_{\epsilon_d} = \frac{1}{N} \sum_{i=1}^N \left(\frac{(\tilde{\epsilon}_d)_i - (\hat{\epsilon}_d)_i}{(\tilde{\epsilon}_d)_i} \right)^2 \quad (24)$$

Appendix F

Figs. F1 and F2 show the results of the three-stage calibration process on the EVP-CD model at 900°C and 1000°C, respectively. Similarly, Figs. F3 and F4 show the results of the calibration process on the EVP-WD model at 900°C and 1000°C, respectively.

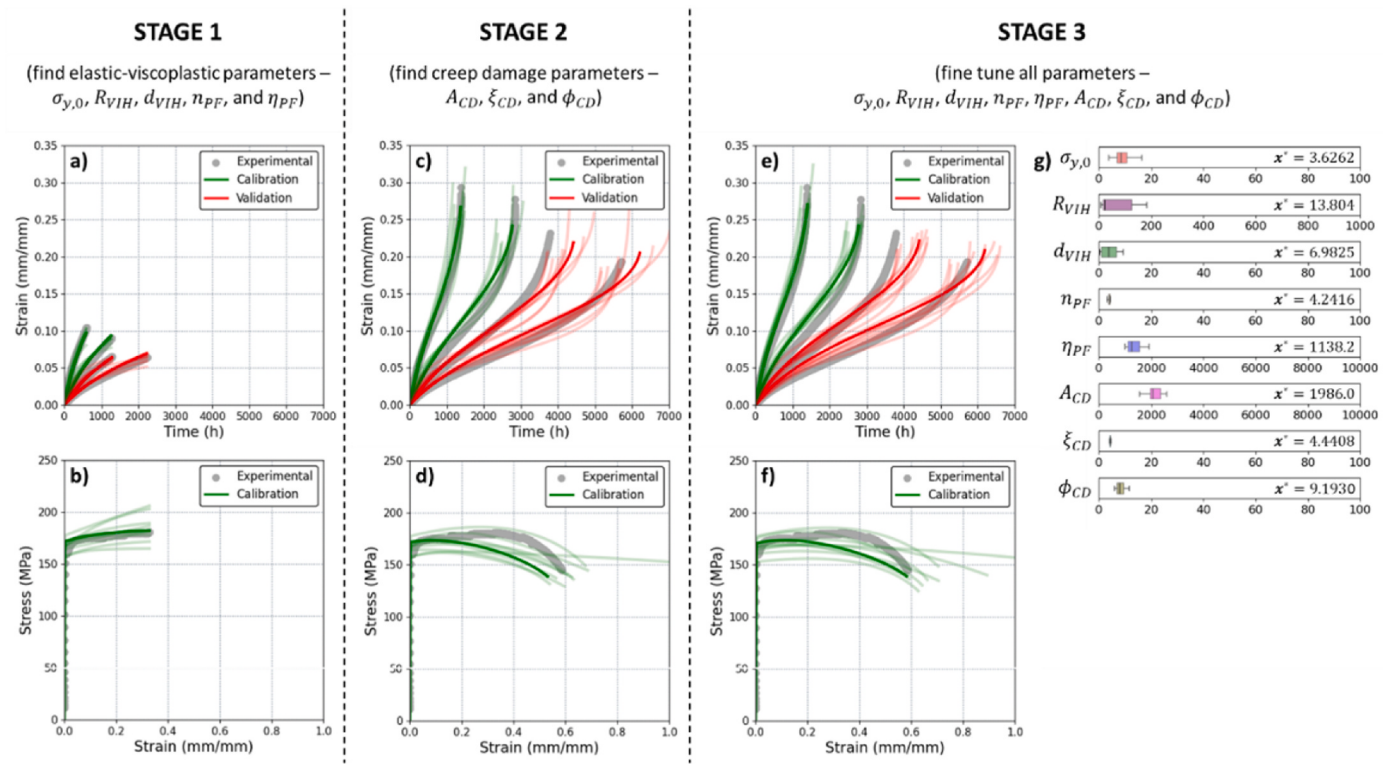


Fig. F1. Optimisation results for the EVP-CD model at 900°C, calibrated with short-term creep curves (36MPa and 31MPa) and tensile curve, and validated with longer-term creep curves (28MPa and 26MPa). The top row of plots (a, c, e) shows the creep results while the bottom row of plots (b, d, and f) shows the tensile results after stages 1, 2, and 3. The experimental datasets are in grey, the simulated curves used for calibration are in green, and the simulated curves used for validation are in red. The boxplots (g) show the distribution of the found parameters, where x^* represents the optimal parameter value, the vertical line represents the mean, the boxes represent the standard deviations, and the whiskers represent the ranges.

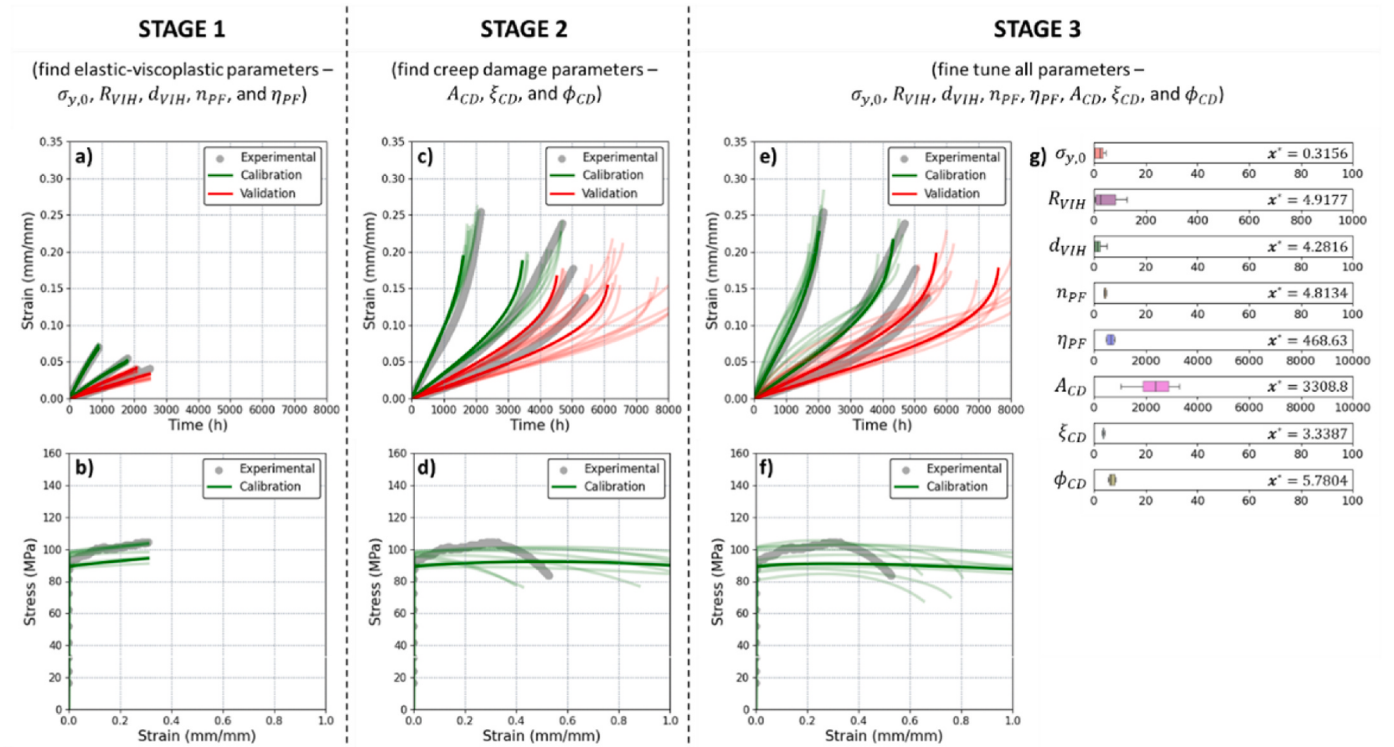


Fig. F2. Optimisation results for the EVP-CD model at 1000°C, calibrated with short-term creep curves (16MPa and 13MPa) and tensile curve, and validated with longer-term creep curves (12MPa and 11MPa). The top row of plots (a, c, e) shows the creep results while the bottom row of plots (b, d, and f) shows the tensile results after stages 1, 2, and 3. The experimental datasets are in grey, the simulated curves used for calibration are in green, and the simulated curves used for validation are in red. The boxplots (g) show the distribution of the found parameters, where x^* represents the optimal parameter value, the vertical line represents the mean, the boxes represent the standard deviations, and the whiskers represent the ranges.

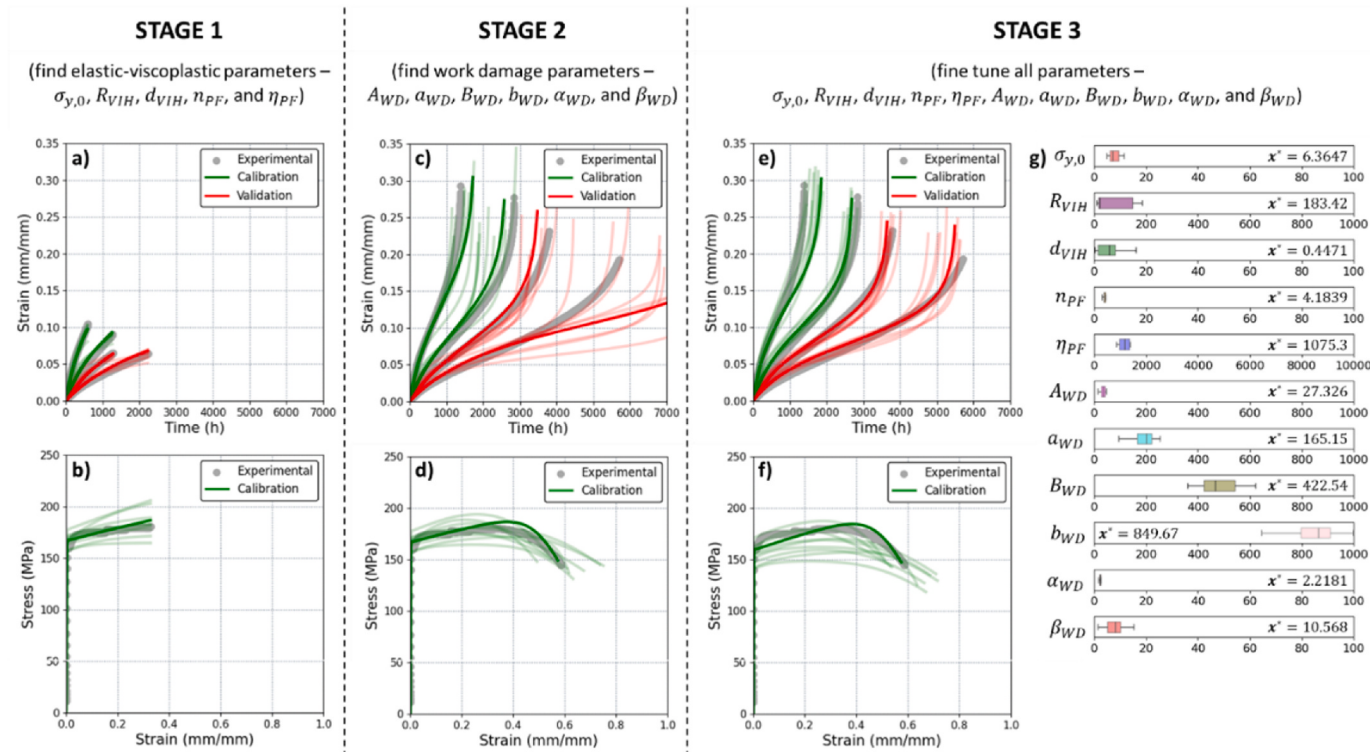


Fig. F3. Optimisation results for the EVP-WD model at 900°C, calibrated with short-term creep curves (36MPa and 31MPa) and tensile curve, and validated with longer-term creep curves (28MPa and 26MPa). The top row of plots (a, c, e) shows the creep results while the bottom row of plots (b, d, and f) shows the tensile results after stages 1, 2, and 3. The experimental datasets are in grey, the simulated curves used for calibration are in green, and the simulated curves used for validation are in red. The boxplots (g) show the distribution of the found parameters, where x^* represents the optimal parameter value, the vertical line represents the mean, the boxes represent the standard deviations, and the whiskers represent the ranges.

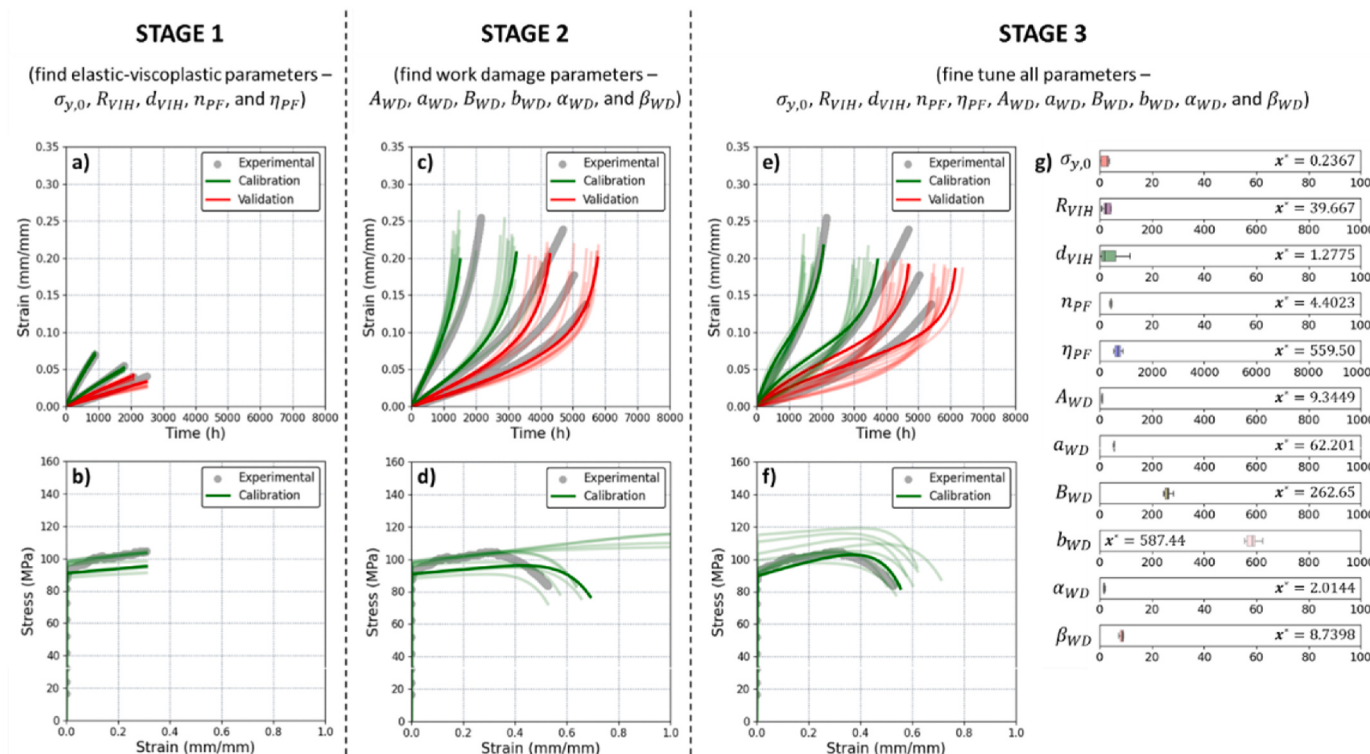


Fig. F4. Optimisation results for the EVP-WD model at 1000°C, calibrated with short-term creep curves (16MPa and 13MPa) and tensile curve, and validated with longer-term creep curves (12MPa and 11MPa). The top row of plots (a, c, e) shows the creep results while the bottom row of plots (b, d, and f) shows the tensile results after stages 1, 2, and 3. The experimental datasets are in grey, the simulated curves used for calibration are in green, and the simulated curves used for validation are in red. The boxplots (g) show the distribution of the found parameters, where x^* represents the optimal parameter value, the vertical line represents the mean, the boxes represent the standard deviations, and the whiskers represent the ranges.

Appendix G

Table G1 and Table G2 contain the best of the material parameters for the EVP-CD model at 800°C, 900°C, and 1000°C found from the three-stage calibration process. Note that the descriptions and units for the material parameters can be found in Table B1.

Table G1

Material parameters from the best calibration run for the EVP-CD model at 800°C, 900°C, and 1000°C.

Temperature	$\sigma_{y,0}$	R_{VIH}	d_{VIH}	n_{PF}	η_{PF}	A_{CD}	ξ_{CD}	ϕ_{CD}
800°C	23.304	276.66	0.32123	4.2592	1767.2	2168.5	5.3181	6.7619
900°C	3.6262	13.804	6.9825	4.2416	1138.2	1986.0	4.4408	9.1930
1000°C	0.31556	4.9177	4.2816	4.8134	468.63	3308.8	3.3387	5.7804

Table G2

Material parameters from the best calibration run for the EVP-WD model at 800°C, 900°C, and 1000°C.

Temperature	$\sigma_{y,0}$	R_{VIH}	d_{VIH}	n_{PF}	η_{PF}	A_{WD}	a_{WD}	B_{WD}	b_{WD}	α_{WD}	β_{WD}
800°C	22.154	462.34	0.17408	4.314	1828.1	40.1	260.65	408.44	853.65	1.9241	7.7562
900°C	6.3647	183.42	0.44712	4.1839	1075.3	27.326	165.15	422.54	849.67	2.2181	10.568
1000°C	0.2367	39.667	1.2775	4.4023	559.5	9.3449	62.201	262.65	587.44	2.0144	8.7398

Data availability

Data will be made available on request.

References

- [1] M.D. McMurtrey, M.P. Heighes, Summary of Alloy 617 and Alloy 709 Elevated Temperature Crack Growth Test Results from the Planned FY24 Crack Growth Test Activities, United States, 2024.
- [2] E.K. Worsham, Decarbonizing Industrial Heat and Electricity Applications Using Advanced Nuclear Energy, 2025. United States.
- [3] A. Nuclear Energy, Beyond Electricity the Economics of Nuclear Cogeneration, OECD Publishing, Paris, 2022.
- [4] OECD, N.E. Agency, Advanced Nuclear Reactor Systems and Future Energy Market Needs, 2021.
- [5] R.N. Wright, Draft ASME Boiler and Pressure Vessel Code Cases and Technical Bases for Use of Alloy 617 for Constructions of Nuclear Component under Section III, Division 5, United States, Size, 2021, p. 384. Medium.
- [6] J. Avila Molina, O. Muránsky, L. Bortolan Neto, J.J. Kružic, R.N. Wright, Development and performance of data-driven models for the prediction of the high-temperature fatigue life of alloy 617, Int. J. Pres. Ves. Pip. 206 (2023) 105022.
- [7] F.H. Norton, The Creep of Steel at High Temperatures, McGraw-Hill book Company, 1929.
- [8] F.R. Larson, J. Miller, A time-temperature relationship for rupture and creep stresses, Transactions of ASME 74 (1952) 765.
- [9] S.S. Manson, A.M. Haferd, A linear time-temperature relation for extrapolation of creep and stress-rupture data, National Advisory Committee for Aeronautics 2890 (1953) 1–49.
- [10] J. Choi, L. Bortolan Neto, R.N. Wright, J.J. Kružic, O. Muránsky, On the prediction of creep behaviour of alloy 617 using Kachanov-Rabotnov model coupled with multi-objective genetic algorithm optimisation, Int. J. Pres. Ves. Pip. 199 (2022) 104721.
- [11] A. Venkataraman, M. Messner, An Initial Framework for the Rapid Qualification of Long-Term Creep Rupture Strength via Microstructural Modeling, Office of Scientific and Technical Information (OSTI), 2021.
- [12] L.M. Kachanov, Time of the rupture process under creep conditions, izvestiya Akademii Nauk SSSR, Otdelenie Tekhnicheskikh Nauk 8 (1958) 26–31.
- [13] Y.N. Rabotnov, F.A. Leckie, W. Prager, Creep problems in structural members, J. Appl. Mech. 37 (1) (1970) 249, 249.
- [14] X.-C. Zhang, J.-G. Gong, F.-H. Gao, F.-Z. Xuan, An improved creep-fatigue life model involving the cyclic softening/hardening and stress relaxation effect, J. Pressure Vessel Technol. 143 (4) (2021).
- [15] N.A. Alang, N.A. Razak, Application of ductility exhaustion based damage model to predict creep rupture time of grade 92 steel, IOP Conf. Ser. Mater. Sci. Eng. 670 (1) (2019) 012001.
- [16] K. Kan, O. Muránsky, P.J. Bendeich, R.N. Wright, J.J. Kružic, W. Payten, Assessment of creep damage models in the prediction of high-temperature creep behaviour of Alloy 617, Int. J. Pres. Ves. Pip. 177 (2019) 103974.
- [17] H. Li, F. Larsson, M.H. Colliander, M. Ekh, Elastic-viscoplastic self-consistent modeling for finite deformation of polycrystalline materials, Mater. Sci. Eng., A 799 (2021) 140325.
- [18] H. Zhang, X. Mao, S. Xu, N. Xiao, N. Zhang, Z. Cui, A physically based elasto-viscoplastic constitutive model for modeling the hot deformation and microstructure evolution of a near α Ti alloy, Mater. Sci. Eng., A 872 (2023) 144994.
- [19] J.D. Robson, D. Armstrong, J. Cordell, D. Pope, T.F. Flint, Calibration of constitutive models using genetic algorithms, Mech. Mater. 189 (2024) 104881.
- [20] H. Tran, Q. Du, G. Zhang, Convergence Analysis for a Nonlocal Gradient Descent Method via Directional Gaussian Smoothing, 2023. ArXiv abs/2302.06404.
- [21] T. Chen, M.C. Messner, Training material models using gradient descent algorithms, Int. J. Plast. 165 (2023) 103605.
- [22] K. Sedighiani, M. Diehl, K. Traka, F. Roters, J. Sietsma, D. Raabe, An efficient and robust approach to determine material parameters of crystal plasticity constitutive laws from macro-scale stress-strain curves, Int. J. Plast. 134 (2020) 102779.
- [23] J. Fernández, J. López-Campos, A. Segade Robleda, J.A. Vilán, A genetic algorithm for the characterization of hyperelastic materials, Appl. Math. Comput. 329 (2018) 239–250.
- [24] J. Wang, W. Jiang, Numerical assessment on fatigue damage evolution of materials at crack tip of CT specimen based on CPFEM, Theor. Appl. Fract. Mech. 109 (2020) 102687.
- [25] P.T.N. Nguyen, F. Abbès, J.S. Lecomte, C. Schuman, B. Abbès, Inverse identification of single-crystal plasticity parameters of HCP zinc from nanoindentation curves and residual topographies, Nanomaterials 12 (3) (2022).
- [26] Y. Lin, W. Yang, Application of multi-objective genetic algorithm based simulation for cost-effective building energy efficiency design and thermal comfort improvement, Front. Energy Res. 6 (2018).
- [27] J.K. Wright, L.J. Carroll, R.N. Wright, Creep and Creep-Fatigue of Alloy 617 Weldments, Office of Scientific and Technical Information (OSTI), 2014.
- [28] J.K. Wright, Next Generation Nuclear Plant Intermediate Heat Exchanger Materials Research and Development Plan (PLN-2804), Office of Scientific and Technical Information (OSTI), 2008.
- [29] J.K. Benz, L.J. Carroll, J.K. Wright, R.N. Wright, T.M. Lillo, Threshold stress creep behavior of alloy 617 at intermediate temperatures, Metall. Mater. Trans. 45 (7) (2014) 3010–3022.
- [30] M.D. McMurtrey, M.P. Heighes, C.J. Gibson, Results of FY 2023 Alloy 617 and Alloy 709 High-Temperature Crack-Growth Testing, United States, 2023.
- [31] ASTM E 139-11, Standard Test Methods for Conducting Creep, Creep-Rupture, and Stress Rupture Tests of Metallic Materials, ASTM International, 2011.
- [32] ASTM E 8-11, Standard Test Methods for Tension Testing of Metallic Materials, ASTM International, 2011.
- [33] C. Jang, S.H. Kim, I. Sah, D. Kim, Creep behavior of Alloy 617 in high temperature air and helium environments—effect of oxidation damage, J. Mech. Sci. Technol. 30 (10) (2016) 4433–4438.
- [34] W.-G. Kim, S.-N. Yin, G.-G. Lee, Y.-W. Kim, S.-J. Kim, Creep oxidation behaviour and creep strength prediction for Alloy 617, Int. J. Pres. Ves. 87 (6) (2010) 289–295.
- [35] L.J. Carroll, C. Cabet, M.C. Carroll, R.N. Wright, The development of microstructural damage during high temperature creep-fatigue of a nickel alloy, Int. J. Fatig. 47 (2013) 115–125.
- [36] W. Sumelka, T. Łodygowski, Viscoplasticity, in: H. Altenbach, A. Öchsner (Eds.), Encyclopedia of Continuum Mechanics, Springer Berlin Heidelberg, Berlin, Heidelberg, 2018, pp. 1–5.
- [37] NEML, The Nuclear Engineering Material Model Library, Argonne National Laboratory, 2024.

- [38] O.M. Heeres, A.S.J. Suiker, R. de Borst, A comparison between the Perzyna viscoplastic model and the Consistency viscoplastic model, *Eur. J. Mech. Solid.* 21 (1) (2002) 1–12.
- [39] E. Krempf, K. Ho, The modeling of inelastic compressibility and incompressibility using the viscoplasticity theory based on overstress (VBO), in: M.F. Hassan, S. M. Megahed (Eds.), *Current Advances in Mechanical Design and Production VII*, Pergamon, Oxford, 2000, pp. 151–160.
- [40] R.A. Leibsohn, A.K. Kanjarla, P. Eisenlohr, An elasto-viscoplastic formulation based on fast Fourier transforms for the prediction of micromechanical fields in polycrystalline materials, *Int. J. Plast.* 32–33 (2012) 59–69.
- [41] P. Perzyna, Fundamental problems in viscoplasticity, in: G.G. Chernyi, H. L. Dryden, P. Germain, L. Howarth, W. Olszak, W. Prager, R.F. Probstein, H. Ziegler (Eds.), *Advances in Applied Mechanics*, Elsevier, 1966, pp. 243–377.
- [42] E. Voce, The relationship between stress and strain for homogeneous deformation, *J. Inst. Met.* 74 (1948) 537–562.
- [43] M. Messner, S. Sham, Draft Pvp2021-61607 A Viscoplastic Model For Alloy 617 For Use With The Asme Section Iii, Division 5 Design By Inelastic Analysis Rules, 2021.
- [44] A.R. Hartloper, A. De Castro E Sousa, D.G. Lignos, Constitutive modeling of structural steels: nonlinear isotropic/kinematic hardening material model and its calibration, *J. Struct. Eng.* 147 (4) (2021) 04021031.
- [45] F.A. Leckie, D.R. Hayhurst, Constitutive equations for creep rupture, *Acta Metall.* 25 (9) (1977) 1059–1070.
- [46] V.-T. Phan, M. Messner, S. Sham, A Unified Engineering Inelastic Model for 316H Stainless Steel, 2019.
- [47] K. Deb, A. Pratap, S. Agarwal, T. Meyarivan, A fast and elitist multiobjective genetic algorithm: NSGA-II, *IEEE Trans. Evol. Comput.* 6 (2) (2002) 182–197.
- [48] J. Blank, K. Deb, Pymoo: multi-objective optimization in Python, *IEEE Access* 8 (2020) 89497–89509.
- [49] M.C. Messner, V.T. Phan, T.L. Sham, Evaluating and modeling rate sensitivity in advanced reactor structural materials: 316H, Gr. 91, and A617, *Int. J. Pres. Ves.* Pip. 178 (2019) 103997.
- [50] M.C. Messner, T.-L. Sham, Reference constitutive model for Alloy 617. 316H Stainless Steel for Use with the ASME Division 5 Design by Inelastic Analysis Rules, Size, United States, 2021, p. 68. Medium.
- [51] C.M. Stewart, A.P. Gordon, Strain and damage-based analytical methods to determine the kachanov–Rabotnov tertiary creep-damage constants, *Int. J. Damage Mech.* 21 (8) (2012) 1186–1201.
- [52] F. Riedlberger, T. Wojcik, R. Buzolin, G. Zuderstorfer, M. Speicher, C. Sommitsch, B. Sonderegger, Microstructural insights into creep of Ni-based alloy 617 at 700 °C provided by electron microscopy and modelling, *Mater. Char.* 198 (2023) 112720.
- [53] X. Wang, L. Xu, L. Jiao, J. Mei, Y. Zhao, L. Qiao, Microstructure evolution during aging and its effect on mechanical properties of a novel nano-carbide dispersion strengthened steel, *Mater. Sci. Eng., A* 928 (2025) 148064.
- [54] T.-H. Feng, X.-F. Xie, Y. Liu, J.-L. Qu, S.-M. Lyu, J.-H. Du, J.-J. Ruan, L.-L. Zhu, Effects of solution treatment on microstructure evolution and the mechanical properties of GH4780 superalloy, *Materials* 18 (6) (2025) 1288.
- [55] S. Zheng, H. Yu, X. Tang, J. Zhou, C. Lu, Y. Li, Y. He, Z. Gao, Effect of phase transformation on the high-temperature tensile behaviors of SA508 Gr. 3 steel: a crystal plasticity finite element investigation, *Nucl. Eng. Des.* 438 (2025) 114070.